CrossMark

JM PAPERS

Influence of particle polydispersity on bulk migration and size segregation in channel flows

Nathan J. Di Vaira[1], **Łukasz Łaniewski-Wołłk**[1,2], **Raymond L. Johnson Jr.**[3], **Saiied M. Aminossadati**[1] **and Christopher R. Leonardi**[1,3,†]

[1]School of Mechanical and Mining Engineering, The University of Queensland, Brisbane, QLD 4072, Australia

[2]Institute of Aeronautics and Applied Mechanics, Warsaw University of Technology, Warsaw 00-665, Poland

[3]Centre for Natural Gas, The University of Queensland, Brisbane, QLD 4072, Australia

The shear-induced migration of dense suspensions with continuously distributed (polydisperse) particle sizes is investigated in planar channel flows for the first time. A coupled lattice Boltzmann–discrete element method numerical framework is employed and validated against benchmark experimental results of bulk shear-induced migration and segregation by particle size. Distinct dependence on the particle size distribution is shown in the flowing (non-plugged) regime (where the bulk solid volume fraction, $\bar{\phi}$, ≤ 0.3) resulting from a dual dependence on the particle self-diffusivity and local rheology imposed by the particle pressure gradient. Close agreement between statistically equivalent bidisperse and polydisperse suspensions suggests that the bulk migration, and by extension the shear-induced diffusivity, is completely characterised by the first three statistical moments of the particle size distribution. For both bidisperse and polydisperse suspensions in the plugging regime, $\bar{\phi} \geq 0.4$, the smallest particles preferentially form the plugs, causing the largest particles to segregate to the channel walls. This effect is accentuated as $\bar{\phi}$ increases and has not been reported in the literature hitherto. It is proposed that smaller particles preferentially form the plugs due to their higher shear-rate fluctuations, which completely dominate particle motion near the plug where the mean shear rate vanishes. Finally, increasing inertia causes a greater bulk migration towards the channel walls, but increased mid-plane migration for the largest particles due to the dependence of the particle self-diffusivity on the particle Reynolds number. As $\bar{\phi}$ increases shear-induced migration dominates and these inertial effects disappear, as does dependence on the particle size distribution.

Key words: suspensions, computational methods, particle/fluid flow

† Email address for correspondence: c.leonardi@uq.edu.au

1. Introduction

Shear-induced migration (SIM) arises in sheared flows as particles deviate from hydrodynamic streamlines due to particle collisions. These accumulated fluctuations result in a particle self-diffusivity in the direction of diminishing shear rate, which scales linearly with the shear rate, $\dot{\gamma}$, and quadratically with the particle radius, a (Leighton & Acrivos 1987). For Poiseuille flows this self-diffusivity causes an accumulation of particles at the channel mid-plane, herein referred to as bulk migration. In suspensions containing particles of two (bidisperse) or more (polydisperse) different size species it also leads to segregation of particles by size, commonly termed size segregation. These phenomena are exploited in the separation of certain cell types from whole blood in microfluidic devices (van Dinther *et al.* 2013; Zhou *et al.* 2019), while size segregation in blood vessels (margination) is critical to effective immune response (Henriquez Rivera, Zhang & Graham 2016) and drug delivery (Müller, Fedosov & Gompper 2016). The blood-cell concentration (haematocrit) can approach 0.54 (Pocock *et al.* 2013), yet there is little understanding of cell segregation at this upper limit of solid volume fraction. In industrial settings, size segregation is employed in microfiltration (Kromkamp *et al.* 2002), while polydisperse mixtures are ubiquitous in geological applications such as hydraulic fracturing (Medina *et al.* 2018).

SIM in regions of homogeneous flow is classically modelled using the suspension balance model (SBM) (Nott & Brady 1994; Morris & Boulay 1999; Miller & Morris 2006), which solves the mass and momentum conservation equations for both the suspension and particle phases. The shear stress, $\tau \sim \eta_s(\phi)\eta_f\dot{\gamma}$, and gradient-direction normal stress (particle pressure), $\Pi \sim \eta_n(\phi)\eta_f|\dot{\gamma}|$, require an adequate rheological model for the local shear and normal suspension dynamic viscosities, $\eta_s(\phi)$ and $\eta_n(\phi)$ (Vollebregt, van der Sman & Boom 2010), where η_f is the dynamic viscosity of the suspending fluid. The macroscopic friction follows, $\mu(\phi) = \tau/\Pi = \eta_s/\eta_n$, and the cross-channel concentration variation itself can be determined by inverting $\mu(\phi)$ (Guazzelli & Pouliquen 2018). The SBM intuitively explains that spatial gradients in the particle pressure drive spatial variations in the particle concentration, due to the dependence of the suspension viscosity on the local solid volume fraction, ϕ (Krieger & Dougherty 1959); here, ϕ is distinguished from the bulk solid volume fraction, $\bar{\phi}$. For pressure-driven Poiseuille flow, as the linear fluid shear gradient develops, a gradient in Π is also created. Further development of the suspension towards its steady-state profile – where Π is constant across the channel width – then drives $\eta_n(\phi)$ (and hence ϕ) to increase towards the channel mid-plane, in the direction in which $\dot{\gamma}$ decreases. This process is herein referred to as viscous suspension reordering, with this general description of SIM herein termed the homogeneous rheology approach. For a critical review of the fundamental physics and modelling of homogeneous SIM the reader is referred to Vollebregt *et al.* (2010). There also exists a simplified, phenomenological version of the SBM, which preceded it in development, named the diffusive flux model (DFM), which relies on diffusion coefficients for the concentration and shear gradients (Phillips *et al.* 1992).

For bidisperse suspensions, the preferential migration of larger particles to the mid-plane, due to their higher self-diffusivity, will be constrained by the local viscosity requirement imposed by the particle pressure. Experiments of Brownian (Semwogerere & Weeks 2008; van Dinther *et al.* 2013) and non-Brownian (Lyon & Leal 1998*b*) suspensions, as well as numerical models (Chun *et al.* 2019; Reddy & Singh 2019), observe that ϕ_L is enriched at the centre of the channel and decreases at the channel walls for all $\bar{\phi}_S/\bar{\phi}_L$, a_S/a_L and $\bar{\phi}$. Here, ϕ_S and ϕ_L are the local solid volume fractions of small and large particles; $\bar{\phi}_S$ and $\bar{\phi}_L$ are the respective bulk solid volume fractions; and a_S and a_L are

the respective particle radii. While ϕ_S remains relatively constant over the width of the channel in most cases, small particles do form a concentration peak at the channel centre for $\bar{\phi}_S > \bar{\phi}_L$ (Semwogerere & Weeks 2008; van Dinther *et al.* 2013; Reddy & Singh 2019), or for $\bar{\phi}_S \geq \bar{\phi}_L$ when $\bar{\phi} = 0.4$ (Lyon & Leal 1998*b*).

A complete description of bidisperse SIM requires a numerical solution of the particle normal stresses. The DFM has been extended to bidisperse suspensions, incorporating a correlation for bidisperse effective viscosity (Shauly, Wachs & Nir 1998). The SBM has also been extended to bidisperse suspensions with the use of a granular temperature, T, which was adopted to sheared granular suspensions from gas kinetic theory (Jenkins & McTigue 1990; Nott & Brady 1994; Morris & Brady 1998); T represents the specific kinetic energy for particle fluctuations and scales with the square of particle size, consequently reproducing the dependence of self-diffusivity on particle size. For bidisperse suspensions, a single effective temperature, T_{eff}, has been utilised in the SBM, where the particle pressure is a linear function of T_{eff}. Closure has been achieved such that Π is a linear function of $\eta_n(\phi)$ and $\dot{\gamma}$, but varies highly nonlinearly with ϕ/ϕ_{rcp} (van der Sman & Vollebregt 2012), where ϕ_{rcp} is the random close packing limit. The efficacy of the SBM for bidisperse suspensions therefore depends on the closure relations for $\eta_n(\phi)$ and ϕ_{rcp}, however, accurate prediction of experimental results (Semwogerere & Weeks 2008) has been demonstrated (Vollebregt, van der Sman & Boom 2012). A similar approach for extension to polydisperse suspensions is theoretically possible, however, none such has been developed.

For Poiseuille flows the homogeneous rheology approach of the SBM is useful for conceptualising and predicting the particle distribution in the sheared regions. Approaching the mid-plane, however, the shear rate disappears. If $\bar{\phi}$ is sufficiently large then ϕ reaches the jamming limit, ϕ_m, at some finite distance from the mid-plane. In the region where $\phi > \phi_m$ the suspension behaves as a uniform un-yielded plug. Instead of vanishing as $\dot{\gamma} \rightarrow 0$, however, μ converges to a finite value, μ_m (Pähtz *et al.* 2019), and within the plug particle rearrangements persist, resulting in sub-yielding, where $\mu < \mu_m$. Over-compaction can also occur, where $\phi_m < \phi < \phi_{rcp}$ (Oh *et al.* 2015). This continued motion within the plug is caused by the propagation of particle fluctuations over the plug threshold from the region where $\dot{\gamma} > 0$ (Lecampion & Garagash 2014). Within the plug, therefore, the particle motion solely depends on the fluctuation rate, which scales $\propto \sqrt{T}/a$ (Pähtz *et al.* 2019). Modelling of SIM in Poiseuille flows therefore needs to capture the homogeneous non-zero shear-rate region and the inhomogeneous vanishing shear-rate region (near/in the plug). For a recent approach, along with a survey of past attempts at modelling over-compaction and sub-yielding, the reader is referred to Gillissen & Ness (2020). In this work complex SIM behaviour is observed in the plugged flow regime which has not been reported in existing bidisperse results.

The discussion thus far has regarded SIM in the limit of vanishing inertia, i.e. as the particle Reynolds number approaches zero, $Re_p \rightarrow 0$. For finite Re_p, however, bulk migration and size segregation are also dependent on inertial migration (IM). In dilute Poiseuille flows, for example, in which particle interactions are negligible, particles migrate closer to the channel walls as Re_p (and hence inertia) is increased (Matas, Morris & Guazzelli 2004). Consequently, for non-dilute particle suspensions bulk migration is dependent on a combination of SIM and IM: increasing inertia causes particles to migrate towards the channel walls, while increasing particle interactions move the suspension back towards the mid-plane (Abbas *et al.* 2014; Kazerooni *et al.* 2017). The shear-induced self-diffusivity, however, also increases with Re_p (Kromkamp *et al.* 2005), meaning that the steady-state particle positions are not simply determined by a

linear balance of SIM and IM. For bidisperse and polydisperse suspensions, this also has the consequence that larger particles should exhibit greater SIM compared with smaller particles when the shear rate is increased, due to their comparatively higher Re_p.

An alternative to mechanistic continuum modelling is the direct numerical simulation (DNS) of all hydrodynamic and particle interaction forces, which has only seen application to Poiseuille flows of dense bidisperse suspensions in a single case (Chun *et al.* 2019). In those coupled lattice Boltzmann method–discrete element method (LBM-DEM) simulations, which employed the first-order accurate link-bounce-back method, it was demonstrated that size segregation occurs on a much longer time scale than bulk migration. However, for the parameter ranges tested, smaller particles never migrated to the channel centre, with a significant ϕ_S trough forming which was more accentuated than in prior experimental results (Lyon & Leal 1998*b*; Semwogerere & Weeks 2008; van Dinther *et al.* 2013). It should also be noted that, due to its computational cost, DNS must be applied with finite Reynolds numbers to obtain meaningful length scales. In this work the LBM-DEM is applied to polydisperse suspensions for the first time, utilising the second-order accurate partially saturated method.

The intrinsic importance of the effective suspension viscosity to SIM requires an analysis of polydisperse viscosity also. It is generally known that the viscosity of polydisperse suspensions decreases as the degree of polydispersity increases (Rastogi, Wagner & Lustig 1996; Luckham & Ukeje 1999; Chun *et al.* 2011). Further, for both bidisperse (Chang & Powell 1994) and polydisperse suspensions (Pednekar, Chun & Morris 2018) the viscosity is a function of ϕ_{rcp}, while ϕ_{rcp} is also a function of the first three statistical moments of a particle size distribution (PSD) (Desmond & Weeks 2014). It was subsequently demonstrated that viscosity is therefore also a function of the statistical moments (Gu, Ozel & Sundaresan 2016; Pednekar *et al.* 2018). By extension, the viscosity of a continuous PSD is also equivalent to a statistically similar bidisperse suspension (Pednekar *et al.* 2018). Consequently, this work characterises polydisperse PSDs by their first three statistical moments. The final part of the paper expands on this equivalence theory, suggesting that statistically equivalent bidisperse and polydisperse suspensions exhibit matching SIM in pressure-driven Poiseuille flows, and that the shear-induced diffusivity is also described by the statistical moments as a result.

2. Methodology

2.1. *Numerical model*

The numerical test cell depicted in figure 1 is implemented to study granular particle bulk migration and size segregation. Spheres ranging in radii from a_{min} to a_{max} are suspended in a Newtonian fluid of constant density, ρ, and kinematic viscosity, $\nu = \eta_f/\rho$, and driven by an external body force, akin to a pressure gradient, G, in the x direction of the channel. SIM occurs in the velocity gradient direction, y, transverse to the mean flow direction, x, and neutral direction, z. The boundaries in the x and z directions are periodic, while fixed wall particles of radius $a_w = a_{min}$ bound the flow in the y direction in order to prevent the formation of a single particle layer at the wall, which is considered a numerical artefact of perfectly smooth walls (Yeo & Maxey 2011; Chun *et al.* 2017). The characteristic channel width, W, is defined as the distance between the innermost points of opposing wall spheres.
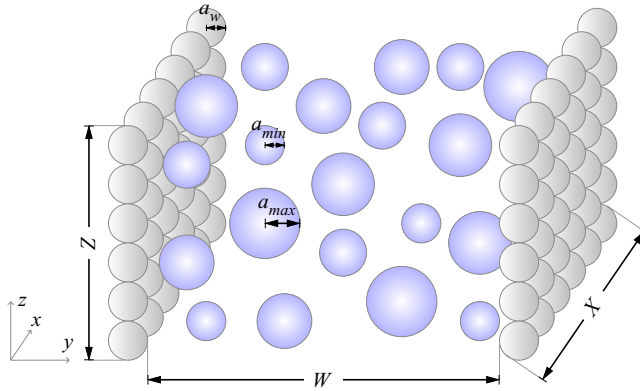
Figure 1. Schematic of the numerical channel used to study the bulk migration and size segregation of polydisperse suspensions with continuous PSDs ranging in radii from a_{min} to a_{max}. Wall particles are stationary with radius a_w. The boundaries are periodic in the x and z directions, while fluid is driven by a constant G in the x direction. Schematic is not to scale.

2.1.1. *Lattice Boltzmann method*

The flow of the suspending fluid is governed by the Navier–Stokes equations for Newtonian fluids,

$$\left.\begin{aligned}
\nabla \cdot \boldsymbol{u} &= 0, \\
\frac{\partial}{\partial t}(\rho \boldsymbol{u}) + \boldsymbol{u} \cdot \nabla(\rho \boldsymbol{u}) &= \nabla p + \nabla \cdot \rho \nu \left[\nabla \boldsymbol{u} + (\nabla \boldsymbol{u})^T\right] + \boldsymbol{F},
\end{aligned}\right\} \tag{2.1}$$

where $\boldsymbol{u}$ is the macroscopic fluid velocity vector and $\boldsymbol{F}$ is the sum of the body force density.

In this study, (2.1) is solved via the lattice Boltzmann method (LBM). The LBM is based on the discrete Boltzmann equation (DBE), which itself discretises the velocity space of the Boltzmann equation into a finite set, $c_i = c_1, \ldots, c_Q$. The DBE is then integrated over discrete points in space, $\boldsymbol{x} + \boldsymbol{c}_i \delta_t$, and time, $t + \delta_t$, to obtain the lattice Boltzmann update equation (LBE),

$$f_i(\boldsymbol{x} + \boldsymbol{c}_i \delta_t, t + \delta_t) = f_i(\boldsymbol{x}, t) - \frac{f_i(\boldsymbol{x}, t) - f_i^{eq}(\rho, \boldsymbol{u})}{\tau} + \mathcal{F}(\boldsymbol{x}, t), \tag{2.2}$$

in which the motion of the fluid is described by the propagation of fluid density distribution functions, f_i, between the discrete lattice of computational nodes along the $\boldsymbol{c}_i$. In this way the LBE retains the properties of implicit integration of the DBE, but is updated via a local and explicit time-stepping scheme, allowing efficient parallelisation on CPU and GPU architectures (Łaniewski-Wołłk 2017). Therefore, while any immersed boundary method coupled with any fluid computational scheme can handle continuously evolving solid boundaries, it is this feature which renders the LBM suitable for large-scale DNS of particle suspensions, and has contributed to its increasing uptake over the last two decades (Kromkamp *et al.* 2006; McCullough *et al.* 2016; Rettinger & Rüde 2018).

Equation (2.2) reflects the single relaxation parameter, τ, used in this work, which relaxes the f_i towards their equilibrium values, f_i^{eq}, in what is known as the Bhatnagar–Gross–Krook collision operator. As the stability of the LBM decreases as $\tau \to 0.5$ and accuracy decreases for $\tau > 1$ in general (Holdych *et al.* 2004), $\tau = 1$ is used in the present study. Here, G is incorporated via the external forcing term, $\mathcal{F}(\boldsymbol{x}, t)$. Twenty-seven velocity directions on a three-dimensional lattice, commonly termed the

*D*3*Q*27 velocity set, are utilised to eliminate spurious velocity currents which potentially arise in the *D*3*Q*15 and *D*3*Q*19 sets.

The macroscopic mass and momentum densities are recovered from the propagation of the mesoscopic f_i,

$$\left.\begin{aligned} \rho(\boldsymbol{x}, t) &= \sum_i f_i(\boldsymbol{x}, t), \\ \rho \boldsymbol{u}(\boldsymbol{x}, t) &= \sum_i \boldsymbol{c}_i f_i(\boldsymbol{x}, t). \end{aligned}\right\} \quad (2.3)$$

In this work, $\nu = 1 \times 10^{-6} \, \mathrm{m^2 \, s^{-1}}$ is first specified, and δ_t is calculated based on,

$$\nu = c_s^2 \left(\tau - \frac{1}{2}\right) \frac{\delta_x^2}{\delta_t}, \quad (2.4)$$

where δ_x is the lattice spacing. A sufficiently small δ_x for numerical accuracy, as shown in § 2.2, is selected. The lattice sound speed, c_s, is equal to $\sqrt{1/3}$ for the isothermal LBM on a square lattice. As with all numerical integration of fluid flows, the maximum stable velocity of the LBM is limited by the speed of information propagation. For bulk flow away from boundaries and $\tau \geq 1$, $C < c_s$ is a sufficient condition for stability, where $C = |\boldsymbol{u}|\delta_t/\delta_x$ is the Courant number. The presence of solid interfaces, however, significantly reduces the limit of this condition and consequently the selection of G in this work. The inferred δ_t and resulting maximum C/c_s are reported in § 2.3. For further introduction to the LBM the interested reader is referred to Kruger *et al.* (2017).

2.1.2. *Discrete element method*

The solid particles of the suspensions are modelled as spheres by the discrete element method (DEM) (Cundall & Strack 1979). The motion of each sphere, *A*, is updated at each discrete time step by explicitly integrating Newton's laws of translational and rotational motion,

$$\left.\begin{aligned} m_A \frac{\mathrm{d}\boldsymbol{u}_A}{\mathrm{d}t} &= \sum_B \left(\boldsymbol{F}_{c,AB}\right) + \boldsymbol{F}_{h,A}, \\ I_A \frac{\mathrm{d}\boldsymbol{\omega}_A}{\mathrm{d}t} &= \sum_B \left(a\boldsymbol{n} \times \boldsymbol{F}_{c,AB}\right), \end{aligned}\right\} \quad (2.5)$$

via a velocity Verlet algorithm, where $\boldsymbol{F}_{c,AB}$ is the force on *A* due to collision with another contacting sphere, *B*. Here, $\boldsymbol{F}_{h,A}$ is the total hydrodynamic force acting on *A*, which is directly calculated by the LBM-DEM coupling method presented in § 2.1.3. No hydrodynamic torque is transmitted to the particles.

The soft sphere interaction model on which the DEM is based replicates particle deformation by allowing the non-deforming spheres to overlap and $\boldsymbol{F}_{c,AB}$ is then calculated as a spring-damper system, based on the sphere–sphere overlap, $\bar{x}$, and relative interaction velocity, $\bar{u}$,

$$\boldsymbol{F}_{c,AB} = (k_n \bar{x}_n - \gamma_n \bar{u}_n) + (k_t \bar{x}_t - \gamma_t \bar{u}_t), \quad (2.6)$$

in which the subscripts *n* and *t* denote the normal and tangential components, respectively. The elastic and damping constants, *k* and γ, are modelled in this work via Hertz contact theory, for which full expressions can be found in Kloss *et al.* (2012). In § 2.2, when the model is validated for SIM of monodisperse suspensions, *k* and γ are tuned by varying the

coefficient of friction and coefficient of restitution. These values of k and γ are then held constant to produce the subsequent results in this work.

The maximum DEM time step for linear collisions,

$$\delta_{t,DEM,max} = \frac{2}{\omega_c}\left(\sqrt{1 + \zeta^2} - \zeta\right), \tag{2.7}$$

provides a guiding criterion for DEM stability, where $\omega_c = \sqrt{k_n/m_{min}}$ is the maximum contact natural frequency and $\zeta = \gamma/(2m_{min}\omega_c)$ is the maximum damping ratio. Equation (2.7), however, neglects the nonlinearity of the Hertz contact model, the additional damping provided by the fluid, as well as the dependence on $\bar{u}$ for large $\bar{u}$ (Burns, Piiroinen & Hanley 2019). Consequently, a safety factor of approximately 0.1 is typically applied if selecting δ_t based on $\delta_{t,DEM}$ (Han, Feng & Owen 2007). In the present work, however, selecting δ_t based on ν and δ_x (as described in § 2.1.1) and utilising $\delta_{t,DEM} = \delta_t$ is sufficient to maintain stability for the range of simulated G. The selected δ_x and inferred δ_t are reported in § 2.3.

2.1.3. *Fluid–solid coupling*

To determine the hydrodynamic force contribution from the LBM to the DEM, and *vice versa*, a coupling method is required. The present model employs the partially saturated method (PSM) (Noble & Torczynski 1998), which falls under the bounce-back (BB) family of LBM boundary schemes. However, the PSM differs from simpler BB schemes in that solid objects are mapped directly to the underlying lattice, with no staircase approximation or interpolation between lattice nodes. The proportion of momentum exchange with each LBM node is instead calculated by overlaying the DEM spheres with the lattice elements and calculating the solid coverage, ε, at each lattice element for each time step, illustrated in two-dimensions by figure 2. Then, ε is converted to the τ-dependent solid weighting function originally presented by Noble & Torczynski (1998),

$$\beta(\tau) = \frac{\varepsilon(\tau - 0.5)}{(1 - \varepsilon) + (\tau - 0.5)}, \tag{2.8}$$

which is applied to (2.2) to obtain a modified LBE,

$$f_i(\boldsymbol{x} + \boldsymbol{c}_i\delta_t, t + \delta_t) = f_i(\boldsymbol{x}, t) - (1 - \beta)\frac{f_i(\boldsymbol{x}, t) - f_i^{eq}(\rho, \boldsymbol{u})}{\tau} + \mathcal{F}(\boldsymbol{x}, t) + \beta\Omega_i^S, \tag{2.9}$$

where Ω_i^S is a new 'solid' collision operator. This work employs the non-equilibrium BB form,

$$\Omega_i^S = f_{-i}(\boldsymbol{x}, t) - f_i(\boldsymbol{x}, t) + f_i^{eq}(\rho, \boldsymbol{u}_s) - f_{-i}^{eq}(\rho, \boldsymbol{u}), \tag{2.10}$$

due to its superior convergence and accuracy over other operators in permeability tests (Wang, Leonardi & Aminossadati 2018). The subscript $-i$ denotes the bounced-back direction, and $\boldsymbol{u}_s$ is the weighted average velocity of all solid objects mapped to the lattice node.

The hydrodynamic force imparted by the fluid on particle A is conveniently calculated by summing contributions of the Ω_i^S from all of the lattice elements, ψ, which map A to the underlying grid,

$$\boldsymbol{F}_{h,A} = \frac{\delta_x^2}{\delta_t}\sum_{\psi}\left(\varepsilon_{\psi}\sum_i\Omega_i^S\boldsymbol{c}_i\right). \tag{2.11}$$

Overall, the PSM effectively interpolates the boundary to calculate the weighted momentum exchange between the fluid and each solid object, while dependence on τ
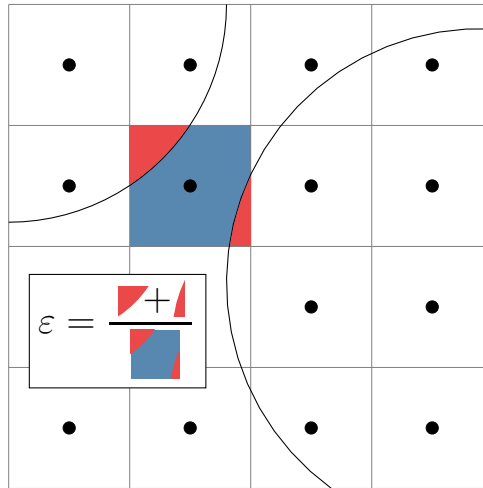
Figure 2. Mapping of DEM spheres to the LBM lattice elements and calculation of the solid coverage, ε, at each lattice element for the PSM.

in maintained. Compared with standard BB, however, which is first-order accurate, the PSM maintains the second-order accuracy of the LBM (Strack & Cook 2007). Further, unlike interpolating methods, it is local, mass conserving and, as all nodes are treated as fluid nodes and information is retained, newly uncovered or covered nodes do not need to be specially treated. Consequently, the PSM has successfully been applied in simulations of dense suspensions across a range of applications (Cook, Noble & Williams 2004; Owen, Leonardi & Feng 2011; Yang *et al.* 2019), and the exact two-way momentum exchange (within second-order accuracy) makes it an excellent candidate to resolve SIM. Implementation of the PSM is achieved via coupling of the open source LBM code base TCLB (Łaniewski-Wołłk & Rokicki 2016) and DEM solver LIGGGHTS (Kloss *et al.* 2012).

2.2. *Verification and validation*

The theoretical second-order numerical accuracy of the PSM is verified via the benchmark case of a single sphere settling between two infinite parallel plates. Initialised at a quarter of the distance between the two plates, the sphere is allowed to settle under the influence of gravity until it reaches a terminal settling velocity due to the inhibiting drag from the plates. The flow around the sphere remains in the Stokes regime. Diffusive scaling is applied to the spatial and temporal resolutions (i.e. $\delta_t \propto \delta_x^2$), which maintains identical physical viscosity between tests in accordance with (2.4). Figure 3 plots the error between the measured terminal velocities for each δ_x and the analytical solution (Faxen 1923), demonstrating second-order convergence with increasing lattice resolution. The lattice nodes per sphere radius, a/δ_x, range from five for the lowest resolution up to 20 for the highest resolution, corresponding to an error range relative to the analytical solution of 0.009–0.2.

Following the model's numerical verification, its ability to accurately capture SIM is validated via comparison with benchmark experimental (Lyon & Leal 1998*a*) and recent LBM-DEM (Chun *et al.* 2017) modelling, as well as the analytical DFM result, for a simple test case comprising monodisperse spheres of radius a. The case parameters are set to $\phi = 0.4$ and $W/a = 44.6$, with periodic dimensions of $X/a = 17.1$ and $Z/a = 11.4$, closely
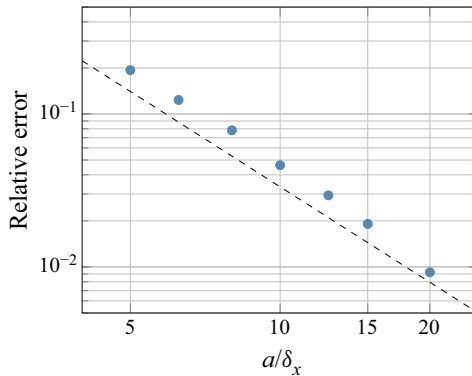
939 A30-8

Figure 3. Log–log plot demonstrating the second-order (dashed line) convergence of the present LBM-DEM model.

emulating the literature studies. A lattice resolution resulting in $a/\delta_x = 5.6$ is utilised. From this validation case, the friction and restitution coefficients of the DEM Hertz contact model are tuned to values of 0.5 and 0.8, respectively.

In figure 4 both ϕ and the suspension velocity, u, normalised by the mean suspension velocity, $\langle u \rangle$, are plotted at points across the channel, y, normalised by the channel width. Overall, the characteristic concentration profile peak and blunted velocity profile are resolved by the present model. The concentration profile is smoother and adheres to the analytical DFM solution more closely compared with the prior LBM work, especially at increasing distance from the channel centre. The concentration depletion at the channel walls seen in the literature LBM results is attributed to measurement of the channel width from $0.25a_w$ within the wall particles. In this study the channel wall is measured from the edge of the wall particles, however, similar concentration depletion occurs if the width plane of reference is extended. Depletion in the experimental results is most likely due to wall roughness. The velocity profile shows close agreement with the literature results but is slightly more blunt. It should also be noted that the experimental results were obtained in the Stokes regime ($Re_{p,LL} = 1.5 \times 10^{-6}$), while the prior and present LBM results were obtained at $Re_{p,LL} = 1.9 \times 10^{-4}$ and 1.4×10^{-3} respectively. This indicates that SIM dominates IM at $\bar{\phi} = 0.4$. Here, the particle Reynolds number is calculated based on the definition in Lyon & Leal (1998a), $Re_{p,LL} = 16\rho a^3 \langle u \rangle / (3\eta_f W^2)$, to allow comparison. An alternative definition of the particle Reynolds number incorporates the local shear rate, which is more indicative of the shear-induced self-diffusivity (Kromkamp *et al.* 2005).

Finally, fundamental cases from the works of Lyon & Leal (1998b) and Chun *et al.* (2019) are reproduced and compared here in order to validate the segregation of particles by size in the present model. These studies were the natural extensions to bidisperse suspensions of their respective prior monodisperse SIM studies (Lyon & Leal 1998a; Chun *et al.* 2017). Both literature studies were at bulk solid volume fraction of $\bar{\phi} = 0.3$, however, the experimental results (Lyon & Leal 1998b) were obtained at $a_L/a_S = 3.4$ and $\bar{\phi}_S/\bar{\phi} = 0.25$, while the numerical LBM and DFM results (Chun *et al.* 2019) were obtained at $a_L/a_S = 1.9$ and $\bar{\phi}_S/\bar{\phi} = 0.33$. Figure 5 compares the results obtained by the present model with both the experimental and numerical literature results. The parameters used to obtain the present model results match the parameters of their respective literature comparison studies, and as such the present model results of figures 5(*a*) and 5(*b*) are quantitatively different. Concentration profiles are shown for half of the channel
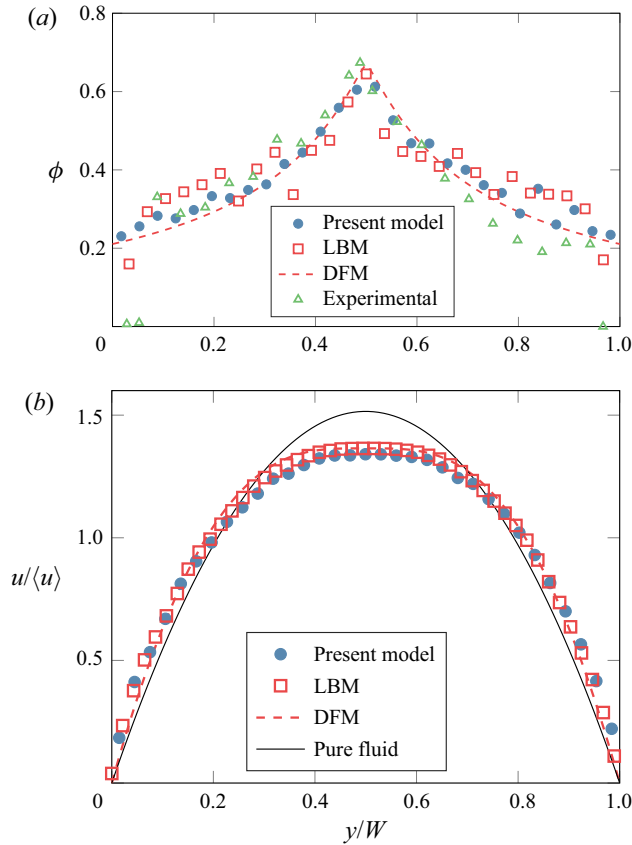
939 A30-9

Figure 4. Validation of SIM for monodisperse suspensions using the presented LBM-DEM model. Comparison of present model with literature LBM, DFM (Chun *et al.* 2017) and experimental (Lyon & Leal 1998*a*) results, as well as pure fluid analytical case, for (*a*) particle concentration profile and (*b*) velocity profile.

($0 < y/W < 0.5$) for clarity. Excellent agreement with Lyon & Leal (1998*b*) and Chun *et al.* (2019) is seen for the concentration of large particles, which attain a maximum concentration in the centre of the channel and a minimum at the channel walls. Small particles, on the other hand, maintain a relatively uniform concentration across the channel, with the present model obtaining a slightly higher concentration at the wall compared with both the experimental and numerical results. It must be noted that all results in figure 5 are obtained at $L/W = 560$, where L is the distance that the suspension has travelled based on the mean suspension velocity. This concept will be discussed further as the distances required for development of size segregation are analysed.

2.3. *Particle distributions and parametrisation*

In the present work five distinct polydisperse PSDs (P_1, P_2, P_3, $P_{2,1}$, $P_{2,2}$) are implemented as the basis for investigating the effect of polydispersity on bulk migration and size segregation. The PSDs are characterised by their first three statistical moments, namely mean, variance and skewness, here denoted by M_1, M_2 and M_3, respectively. The reason for doing so is based on the fact that the rheologies of polydisperse PSDs are completely described by their first three statistical moments, and that bidisperse and
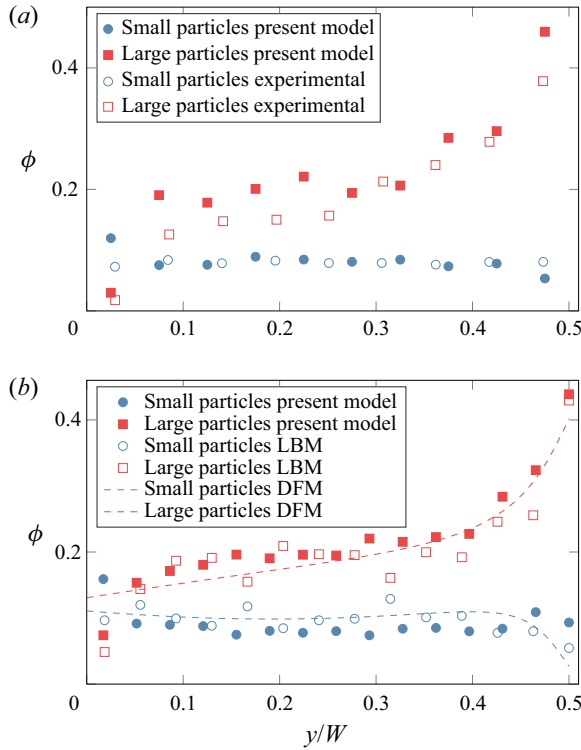
939 A30-10

Figure 5. Validation of particle segregation by size for bidisperse suspensions via comparison with fundamental (*a*) experimental (Lyon & Leal 1998*b*) and (*b*) numerical LBM and DFM (Chun *et al.* 2019) cases.

polydisperse distributions with matching M_1, M_2 and M_3 have identical effective viscosity (Pednekar *et al.* 2018). In this work the bidisperse–polydisperse equivalence is shown to extend to SIM in pressure-driven Poiseuille flows.

A two-parameter Weibull function is used to define the probability density functions, $f(a)$, of the number of particles by particle size,

$$f(a) = \frac{\lambda_1}{\lambda_2} \left(\frac{a}{\lambda_2} \right)^{\lambda_1 - 1} e^{-(a/\lambda_2)^{\lambda_1}}. \tag{2.12}$$

The shape and scale parameters, λ_1 and λ_2, consequently define M_1, M_2 and M_3. The statistical measurements of all PSDs are reported in table 1, which also includes ϕ_{rcp} as calculated from an empirical formula based on the statistical moments (Desmond & Weeks 2014),

$$\phi_{rcp} = \phi_{rcp}^* + c_1 \frac{\sqrt{M_2}}{M_1} + c_2 \frac{M_2 M_3}{M_1^2}, \tag{2.13}$$

where ϕ_{rcp}^* is the maximum random close packing concentration for monodisperse spheres and $c_1 = 0.0658$ and $c_2 = 0.0857$ are empirically determined coefficients. P_1, P_2 and P_3 are designed to have widely varying M_1, M_2, M_3, and consequently ϕ_{rcp}, while P_2, $P_{2,1}$ and $P_{2,2}$ have matching M_1 but significantly different M_2, M_3 and ϕ_{rcp}, in order to isolate any dependence on M_1. Figure 6 plots the $f(a)$ of all PSDs, while figure 7 re-plots the $f(a)$

	λ_1	λ_2	M_1	M_2	M_3	ϕ_{rcp}
P_1	0.6	1.0	1.58	0.30	1.50	0.672
P_2	1.0	1.3	1.88	0.41	0.92	0.666
P_3	1.8	2.0	2.47	0.48	0.17	0.654
$P_{2,1}$	1.2	0.9	1.89	0.58	0.9	0.673
$P_{2,2}$	1.0	1.7	1.89	0.28	0.78	0.658

Table 1. Statistical measurements of the five polydisperse PSDs used in this work. The Weibull parameters, λ_1 and λ_2, define the distributions, which are subsequently characterised by their first three statistical moments, M_1, M_2 and M_3, and the random close packing solid volume fraction, ϕ_{rcp}.
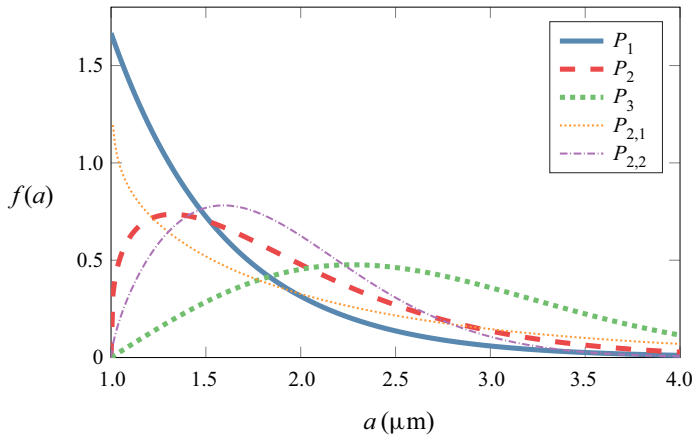
Figure 6. Probability density functions for the five different PSDs tested.
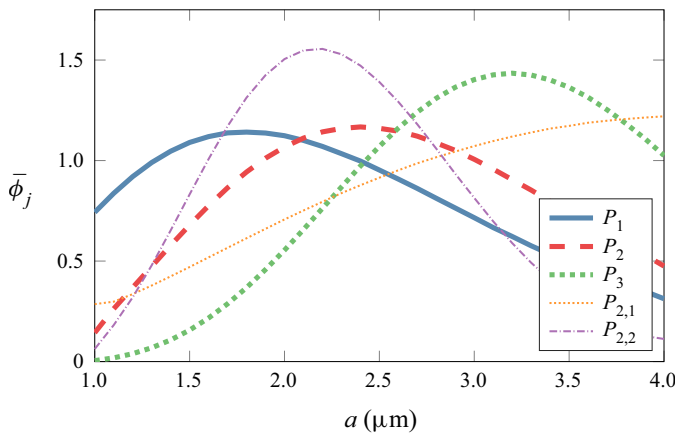
Figure 7. Concentration by particle size of each PSD. Note that $\bar{\phi}_j$ scales arbitrarily.

as the bulk concentration of each particle size, $\bar{\phi}_j$, rather than the number of particles, to give a more meaningful volumetric interpretation when analysing bulk migration and size segregation.

The PSDs are shifted such that $a_{min} = 1\,\mu\text{m}$, and truncated at a maximum of $a_{max} = 3.9\,\mu\text{m}$, such that $a_{max}/a_{min} = 3.9$. It is acknowledged that Brownian and electrostatic

forces could influence results at these particle sizes, however, this is considered outside the scope of the present work. It is also noted that, in the absence of these forces, it is not essential to designate physical length scales to the particles, however, this is done in this work as a matter of style and to increase the ease of interpretation and discussion of the results.

The continuous distributions of particle radii are implemented in the DEM as discrete radii, but in sufficiently small increments of $\delta_a = 0.1\,\mu\text{m}$ so as to closely approximate a continuous distribution. Particle species are defined by particle size, such that all particles comprising a single particle size are designated as a single species, j. With $[a_{min}, a_{max}] = [1, 3.9]\,\mu\text{m}$ and $\delta_a = 0.1\,\mu\text{m}$ there are a total of $K = 30$ particle size species.

As well as varying the PSDs, $\bar{\phi}$ is varied between 0.2 and 0.55. G is varied between 1 and $16\,\text{MPa}\,\text{m}^{-1}$ in order to analyse the competing effects of SIM and IM, and to maintain Re_c in the cases where $\bar{\phi}$ is varied. The degree of inertia is defined by the channel Reynolds number,

$$Re_c = \frac{\rho \langle u \rangle W}{\bar{\eta}_s} = \frac{12\rho \langle u \rangle^2}{GW}, \tag{2.14}$$

where $\langle u \rangle$ is the mean channel suspension velocity. The bulk effective shear viscosity, $\bar{\eta}_s$, is distinguished from the local effective shear viscosity, $\eta_s(\phi)$, as the latter varies locally with the particle size composition. There is no single way to define the channel bulk effective shear viscosity; here $\bar{\eta}_s = GW^2/(12\langle u \rangle)$ is used, analogous to momentum conservation for planar Poiseuille flow.

The numerical domain is held constant for all tests at $W = 100\,\mu\text{m}$, $X = 64\,\mu\text{m}$ and $Z = 38\,\mu\text{m}$. A domain dependence study was performed prior to determining these dimensions, showing that migration is independent of the domain height for $Z \geq 20\,\mu\text{m}$. A lattice spacing of $\delta_x = 0.4\,\mu\text{m}$ is utilised, corresponding to $a_{min}/\delta_x = 2.5$ and $a_{max}/\delta_x = 9.75$. According to (2.4), the inferred $\delta_t = \delta_{t,DEM}$ is therefore $2.667 \times 10^{-8}\,\text{s}$, resulting in $C/c_s \leq 0.233$ and $\delta_{t,DEM}/\delta_{t,DEM,max} \approx 0.2$ (for linear collisions according to (2.7)).

It must also be noted that, between parametrically and statistically identical simulations and distributions with different randomised particle injections, there is appreciable difference in bulk migration and size segregation between the simulations. This reflects the stochastic nature of the accumulated irreversible particle interactions which contribute to SIM. These differences, however, average over all simulations. As such, in some cases the data points are the median of up to ten simulations with randomised injection between each.

3. Results

The degree of SIM of particles of a particular size (i.e. those comprising particle species j) is conveniently measured by the scalar dispersion function,

$$C_j(t) = \frac{1}{N_j} \sum_{i=1}^{N_j} \left| \frac{y_i}{w} - \frac{1}{2} \right|, \tag{3.1}$$

where N_j is the number of particles of species j and y_i is the transverse ordinate of the ith particle in species j. Overall, C_j is the distance from the mid-plane averaged over all particles of species j at each time step. $C_j = 0$ if all particles are positioned exactly in the middle of the channel, while $C_j = 0.5$ if all particles are positioned exactly on the channel walls. It is defined for planar flows only under the assumption that the concentration distribution is approximately symmetric about the mid-plane.

The bulk scalar dispersion function,

$$C(t) = \frac{\sum_{j=1}^{K} C_j \bar{\phi}_j}{\bar{\phi}}, \tag{3.2}$$

is calculated by weighting the C_j of each species by their bulk solid volume fraction, $\bar{\phi}_j$. Due to this weighting, C represents the total dispersion of mass across the channel. $C \to 0$ denotes the channel-averaged particle mass approaching the mid-plane.

To quantify the relative transverse motion of particles of different sizes, and capture the difference in transient behaviour between total and relative particle motion seen in previous bidisperse studies, a scalar segregation function is also defined,

$$C_{\Sigma}(t) = \frac{4}{K} \sum_{i=1}^{K} \left(\frac{1}{K} \sum_{j=1}^{K} |C_i - C_j| \right), \tag{3.3}$$

which takes into account the difference in channel position between particles of all sizes. It is constructed in such a way that, if all particle sizes are distributed in the same manner, $C_{\Sigma} = 0$. If all particles representing half of the size species are positioned in the channel centre, and all particles of the other half of size species are at the channel wall, C_{Σ} attains a maximum value of 1.

The primary scale of interest is the mean length travelled along the channel, L, by the suspension. Due to the discrete nature of the numerical model it may be calculated at each time step,

$$L(t) = \sum_{i=0}^{t} \langle u \rangle_i \Delta t, \tag{3.4}$$

and is expressed throughout the results relative to the channel width, L/W.

3.1. *Distribution (polydispersity)*

The SIM of the five continuous PSDs are firstly compared, at constant parameters of $\bar{\phi} = 0.3$ and $G = 2\,\mathrm{MPa\,m^{-1}}$, to investigate the effect of polydispersity on bulk migration and size segregation. This combination of $\bar{\phi}$ and G results in $Re_c \approx 25$ across all simulations for all PSDs (at $L/W \approx 1800$).

Firstly, the transient development of C depicted in figure 8 suggests that the bulk migration for each PSD reaches steady state after $L/W \approx 600$. The lowest steady state C achieved by P_3 indicates that a higher volume of particles have accumulated at the channel centre, compared with all other PSDs. In other words, the suspension with the highest mean particle size (P_3) has attained the highest degree of bulk migration by particle volume, while the suspension with the lowest mean (P_1) has the most spread particle concentration. While the suspensions with matching mean (P_2, $P_{2,1}$, $P_{2,2}$) have closer C compared with P_1 and P_3, their distinct difference indicates that bulk migration is also a function of the variance and skewness (M_2 and M_3), but to a lesser degree than the mean (M_1).

The scalar bulk migration in figure 8 is commensurate with the plot of concentration profiles for P_1, P_2 and P_3 in figure 9. It is clear that P_3 has a higher particle concentration around the centre of the channel ($0.4 < y/W < 0.6$), but lower at the edges ($y/W < 0.2$, $y/W > 0.8$), compared with P_2 and P_1. The concentration plots for $P_{2,1}$ and $P_{2,2}$ are omitted from figure 9 on the grounds that they closely match that of P_2, as their bulk
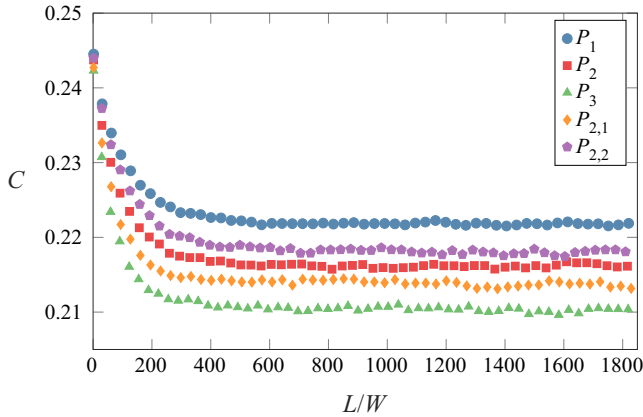
939 A30-14

Figure 8. Development of bulk scalar dispersion function, C, along normalised channel length, L/W. Comparison of each PSD at $\bar{\phi} = 0.3$, $G = 2\,\mathrm{MPa\,m^{-1}}$. Lower C indicates that the channel-averaged particle mass is closer to the channel mid-plane.
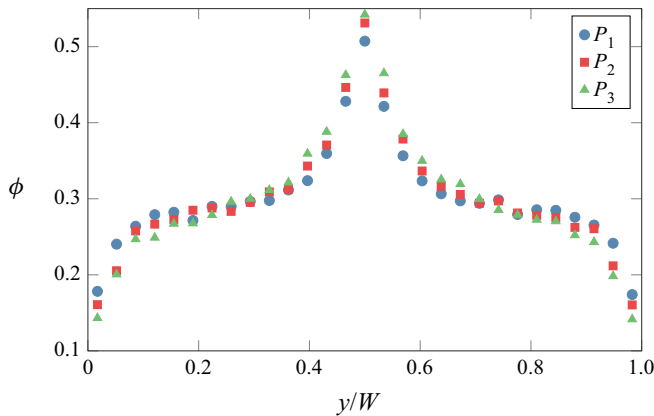

Figure 9. Concentration profiles plotted as solid volume fraction, ϕ, across the normalised channel width, y/W. Comparison of P_1, P_2 and P_3 at $\bar{\phi} = 0.3$, $G = 2\,\mathrm{MPa\,m^{-1}}$, with measurements taken at $L/W \approx 1800$.

migration is similar. Compared with the concentration profile for the monodisperse case in figure 4, the polydisperse suspensions attain significantly sharper concentration peaks which drop away much more at the channel walls. The decreased wall concentration is due to two factors. Firstly, particles become less uniformly distributed near the walls as W/a decreases (Kazerooni *et al.* 2017), and the ratio of W/a_{max} is relatively low in this work. Secondly, interactions with wall particles cause a depletion of the particle concentration near the wall. While decreasing the wall particle size would decrease this depletion effect, at the limit of $a_w \to 0$ the virtually smooth wall would cause a single layer of wall particles to form which is non-physical. In a similar vein a realistic surface roughness, especially of naturally occurring fractures, is self-affine and comprises a range of wavelengths, posing the question of what size is representative (Łaniewski-Wołłk & Leonardi 2020). The scope of this investigation is narrowed by cutting the spectrum of the roughness to wavelengths equal or lower than the smallest particle size, by setting $a_w = a_{min}$. Analysis of varying a_w merits further investigation, but is outside the scope of the current work.
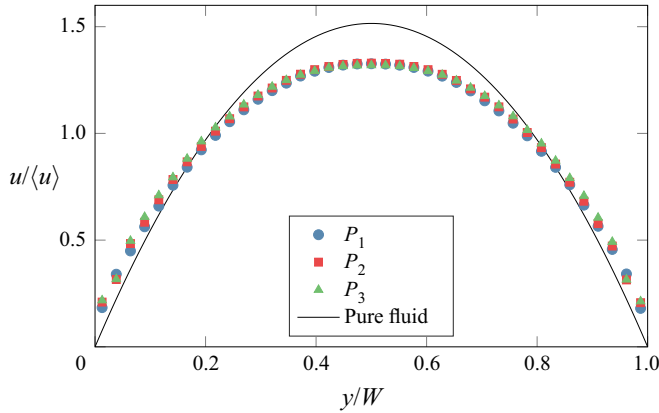
Figure 10. Velocity profile plotted as channel velocity, u, normalised by mean channel velocity, $\langle u \rangle$. Comparison of P_1, P_2 and P_3 at $\bar{\phi} = 0.3$, $G = 2\,\mathrm{MPa\,m^{-1}}$, with measurements taken at $L/W \approx 1800$.
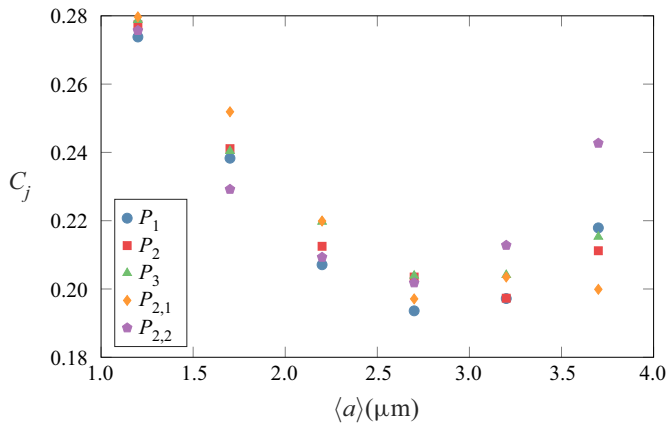

Figure 11. Scalar dispersion function by particle size species, C_j. Comparison of each PSD at $\bar{\phi} = 0.3$, $G = 2\,\mathrm{MPa\,m^{-1}}$, with measurements taken at $L/W \approx 1800$. Particles are grouped into bins by radius of width $0.4\,\mu\mathrm{m}$, recalling that $\delta_a = 0.1\,\mu\mathrm{m}$, and are plotted at their median value, $\langle a \rangle$. Lower C_j indicates particles have migrated closer to the channel mid-plane.

Blunting of the velocity profiles, which is also characteristic of SIM, is demonstrated in figure 10. Unlike the concentration profiles, there is negligible dependence on the PSD for the velocity profiles. This lack of variation due to concentration by particle size is in line with prior bidisperse results (Lyon & Leal 1998b; Chun *et al.* 2019). The slip velocity immediately adjacent to the walls is due to the wall depletion interaction just described.

To analyse the size segregation between individual size species, figure 11 shows C_j over the full range of particle sizes measured at $L/W \approx 1800$. It must first be noted that, while particle sizes are implemented in the DEM in discrete increments of $\delta_a = 0.1\,\mu\mathrm{m}$, C_j is plotted here in particle bins of width $a = 0.4\,\mu\mathrm{m}$. This is primarily done for ease of interpretation and visualisation. Further, the stochastic nature of SIM results in variation of bulk migration and size segregation between parametrically identical simulations, as explained in § 2.3. Consequently, only the median values of C_j are included. A full box and whisker plot showing the variability in the data over all randomised simulations is shown in the Appendix.

939 A30-16

Two significant observations can be made from figure 11. Firstly, for all PSDs, the largest particles do not migrate most to the channel centre relative to all particle sizes. This is especially pronounced for P_1 and $P_{2,2}$, for which the particles of size $2.5 \leq a \leq 2.9\,\mu\text{m}$ attain the highest occupancy at the channel centre. If interpreted via a concentration profile plot, these particles would exhibit a larger peak at the channel centre compared with the largest particles. Secondly, the migration of individual particle sizes differs significantly between PSDs, with this difference being especially pronounced for $P_{2,1}$ and $P_{2,2}$.

The results presented thus far can be analysed in terms of the classical homogeneous rheology description of SIM: as described in § 1, the bulk migration and size segregation of polydisperse suspensions depend on both the particle self-diffusivity and viscous suspension reordering. Due to scaling of the self-diffusivity (granular temperature) with particle size, larger particles will preferentially migrate to the channel mid-plane, however, their migration will be constrained by the local rheological requirements imposed by the particle pressure gradient.

The strong dependence of bulk migration on M_1, for example, is obviously a direct result of the self-diffusivity scaling with particle size; a larger M_1 indicates a higher number of larger particles, and therefore greater bulk migration. The distinct (but smaller) difference in bulk migration between suspensions with matching M_1, however, also indicates a (smaller) dependence of bulk migration on M_2 and M_3. This dependence is intrinsically linked to the size segregation differences in figure 11, which are explained by the viscous suspension reordering. Recalling that the polydisperse ϕ_{rcp} (and consequently $\eta_n(\phi)$) given by (2.13) is a strong function of M_2 and M_3, the local $\eta_n(\phi)$ requirement induced by the particle pressure therefore drives the local particle size composition. For $P_{2,2}$, for example, in order to satisfy the viscosity at every point across the channel width, the few particles of size $3.5 \leq a \leq 4\,\mu\text{m}$ must necessarily migrate away from the mid-plane. Conversely, $P_{2,1}$ contains a comparatively higher concentration of the largest particles, which are therefore free to attain a position closest to the mid-plane, while the smallest particles must be more spread.

Confirmation of this hypothesis requires interrogation of the particle pressure to obtain the self-diffusivity of individual size species and the overall particle pressure gradient, as well as the use of an adequate model of the local suspension rheology. Due to its complexity, however, this type of analysis is left for a future work which may seek to exactly quantify particle diffusion in relation to polydispersity.

To analyse the transient size segregation in greater depth, figure 12 plots the development of C_j along the channel, separated into the same particle bins of width $a = 0.4\,\mu\text{m}$ as in figure 11, for P_1, P_2 and P_3. What emerges is a very different transient response compared with C alone. Most notably, for all three PSDs, the largest particles ($3.5 \leq a \leq 3.9\,\mu\text{m}$) exhibit an initial SIM to a minimum C_j, evidently driven by the self-diffusivity (which scales with particle size). After this initial SIM, however, the largest particles reverse their overall SIM direction (i.e. C_j begins to increase) and they begin to migrate back towards the channel walls due to the viscous suspension reordering. It follows that this reordering of the local particle composition, and hence the long-term size segregation, occurs on a longer time scale than the particle diffusion.

The transient size segregation development is also reflected in the scalar segregation function. The values of C_Σ in figure 13, are commensurate with the trends of C_j for individual particle size species in figure 12. For P_1, C_Σ reaches a maximum at $L/W \approx 400$, which coincides with the reversal of the largest particles in figure 12(a). The value of C_Σ then slowly decreases, never reaching a clear steady state, which corresponds to the slow increase of C_j of the largest particles. For P_2, on the other hand, C_Σ
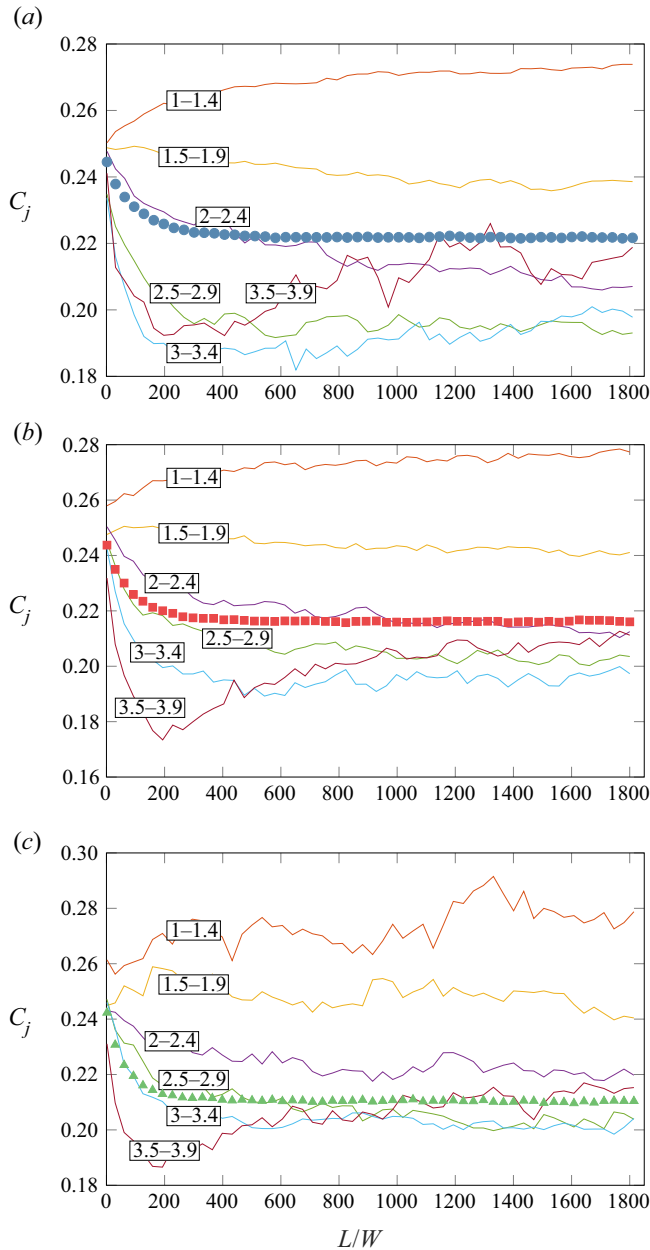
Figure 12. Transient development of scalar dispersion function by particle size species, C_j. Comparison of (*a*) P_1, (*b*) P_2 and (*c*) P_3 at $\bar{\phi} = 0.3$, $G = 2\,\text{MPa}\,\text{m}^{-1}$. Particles are grouped into bins by radius of width $0.4\,\mu\text{m}$, recalling that $\delta_a = 0.1\,\mu\text{m}$. Labels on lines indicate bin size in μm. Markers represent the bulk scalar dispersion of the suspensions, C. Lower C_j and C indicates particles have migrated closer to the channel mid-plane.

appears to reach a constant value at $L/W \approx 800$, which is also evident in figure 12(*b*). As P_3 is composed mainly of larger particles, a trend in C_Σ is harder to distinguish, however, it could reasonably be concluded in conjunction with figure 12(*c*) that steady state is reached at $L/W \approx 600$. Overall, viscous suspension reordering occurs on a longer
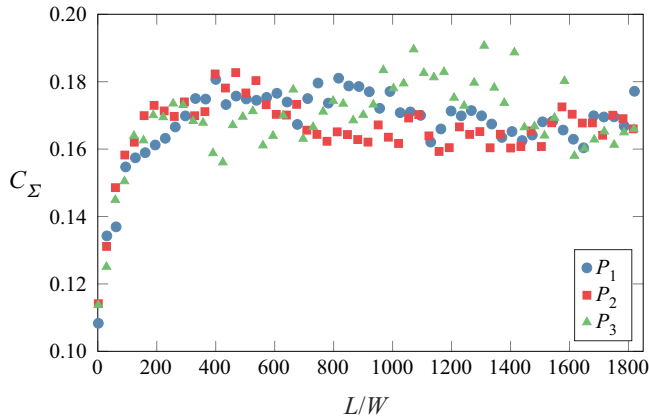
Figure 13. Development of scalar segregation function, C_Σ, along the normalised channel length, L/W, highlighting the transient size segregation behaviour of polydisperse suspensions. Comparison of P_1, P_2 and P_3 at $\bar\phi = 0.3$, $G = 2\,\mathrm{MPa\,m}^{-1}$. Higher C_Σ indicates greater size segregation.

time scale for suspensions containing a larger proportion of smaller particles. These reordering/segregation development lengths also correspond to a range of 1.3–3 times larger than the development lengths for suspension bulk migration. This range of time scale differences is much lower than that previously observed for bidisperse suspensions (Chun *et al.* 2019).

3.2. *Concentration*

The following results investigate the effect of bulk suspension concentration, $\bar\phi$, on particle SIM in polydisperse suspensions. Firstly, concentrations of $\bar\phi = 0.2$, 0.3, 0.4 and 0.5 are tested for P_2 only. The pressure gradient is increased with $\bar\phi$ as $G = 1.1$, 2, 4.25 and $10\,\mathrm{MPa\,m}^{-1}$ in order to obtain a similar Re_c for all $\bar\phi$ ($Re_c = 25$, 25, 25 and 20). The lower value of $Re_c = 20$ for $\bar\phi = 0.5$ is the maximum achievable Re_c while maintaining numerical stability. In § 3.3, however, this small inertial difference is shown to have negligible impact on SIM at $\bar\phi = 0.5$.

Figures 14 and 15 summarise the effect of suspension concentration on bulk migration and size segregation. According to figure 14, at the lowest concentration ($\bar\phi = 0.2$) bulk migration is low (i.e. C is high). There is still size segregation, as shown in the variation of C_j for different particle sizes in figure 15, but the values of C_j are slightly higher compared with $\bar\phi = 0.3$. In figure 14, bulk migration is similar for $\bar\phi = 0.3$ and $\bar\phi = 0.4$, however, as the concentration is further increased to $\bar\phi = 0.5$, C significantly increases again, suggesting that there is a critical bulk concentration at $\bar\phi \approx 0.3 - 0.4$ where a change in behaviour occurs. Figure 15 shows that at this change in behaviour the larger particles migrate closer to the channel walls, relative to smaller particles. This is accentuated as $\bar\phi$ increases. For $\bar\phi = 0.4$, particles of size $2 \leq a \leq 2.4\,\mu\mathrm{m}$ migrate closest to the channel centre, while for $\bar\phi = 0.5$ particles of size $1 \leq a \leq 1.9\,\mu\mathrm{m}$ migrate closest to the channel centre. Figure 16 illustrates this phenomenon, which has not been reported in the literature for dense suspensions hitherto.

The velocity profiles for each $\bar\phi$ are plotted in figure 17. Total flattening of the velocity profiles for $\bar\phi = 0.4$ and 0.5 indicate the regions in which a plug has formed (i.e. ϕ has reached ϕ_m such that the shear rate vanishes). A large plug spanning 1/5 of the channel width forms for $\bar\phi = 0.5$, while a smaller one forms for $\bar\phi = 0.4$. These are indicated on the

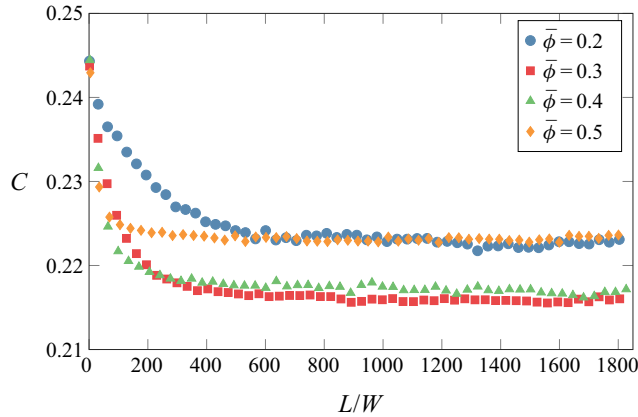Figure 14. Development of bulk scalar dispersion function, C, along normalised channel length, L/W. Comparison of different $\bar{\phi}$ for P_2. Lower C indicates that the channel-averaged particle mass is closer to the channel mid-plane.
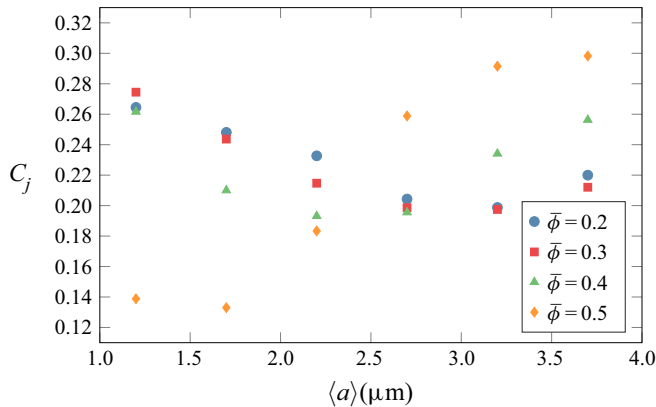

Figure 15. Scalar dispersion function by particle size species, C_j. Comparison of different $\bar{\phi}$ for P_2, measured at $L/W \approx 1800$. Particles are grouped into bins by particle radius of width $0.4\,\mu\text{m}$, recalling that $\delta_a = 0.1\,\mu\text{m}$, and are plotted at their median value, $\langle a \rangle$. Lower C_j indicates particles have migrated closer to the channel mid-plane.

velocity profiles with vertical dashed and dotted lines, respectively. This plug formation at $\bar{\phi} = 0.4$ coincides with the change in behaviour elucidated above.

It is evident that the plugs first form due to bulk migration, and preferentially comprise the smallest sized particles. This then determines which particles compose the sheared region outside the plug, where $\dot{\gamma} > 0$. The larger the plug, the more small particles are required to compose the plug, meaning that more large particles will be closer to the channel walls (i.e. the C_j of large particles, as well as the overall C, will gradually increase as the plug size increases). Figure 18 illustrates how the small particles segregate to form the plugs, and that the length scale on which this size segregation occurs increases significantly as $\bar{\phi}$ increases.

Preferential formation of the plugs with small particles can be explained in terms of particle fluctuations, which propagate into the plug (where $\dot{\gamma} = 0$) from just inside the sheared region (where $\dot{\gamma} > 0$), causing particle rearrangements to persist (Lecampion & Garagash 2014). In the plugged region, particle motions are completely defined by the
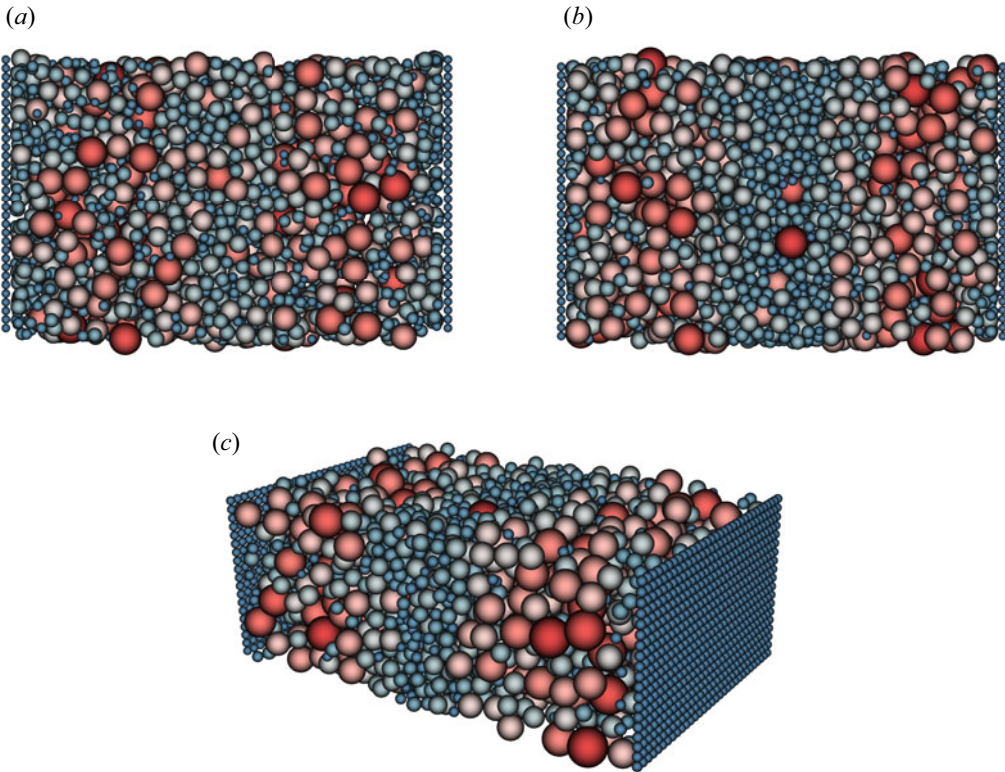
939 A30-20

Figure 16. Graphical representations of (*a*) $\bar{\phi} = 0.4$ *z*-plane, (*b*) $\bar{\phi} = 0.5$ *z*-plane, (*c*) $\bar{\phi} = 0.5$ isometric, captured at $L/W \approx 1800$ for P_2.
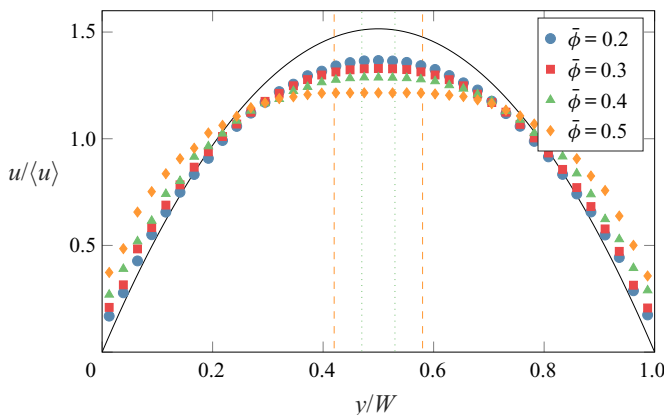

Figure 17. Comparison of velocity profiles for increasing $\bar{\phi}$ for P_2, measured at $L/W \approx 1800$. Plugged regions are indicated by vertical dotted lines for $\bar{\phi} = 0.4$ and vertical dashed lines for $\bar{\phi} = 0.5$.

amplitude of the root mean square of shear-rate fluctuations, $\dot{\gamma}_{rms}$ (Gillissen & Ness 2020). As $\dot{\gamma}_{rms}$ scales inversely with the particle size ($\dot{\gamma}_{rms} \propto \sqrt{T}/a$), it is the small particles which have the greatest motion within the plug (Pähtz *et al.* 2019). Consequently, as the plug forms, it is the smallest particles which will preferentially fluctuate to within the plug. Less formally, based on a simple momentum conservation view, the fluctuation
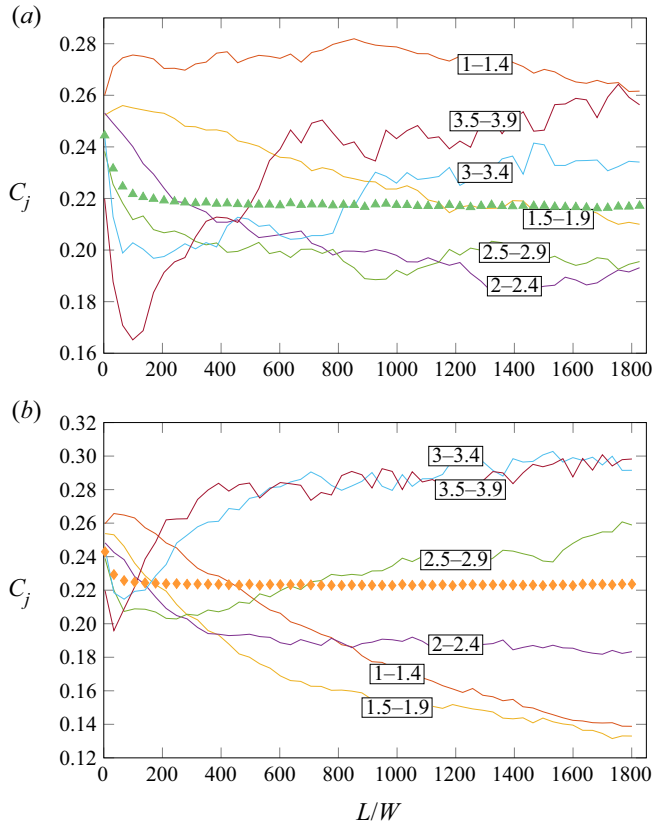
Figure 18. Transient development of scalar dispersion function by particle size species, C_j, for (a) $\bar{\phi} = 0.4$ and (b) $\bar{\phi} = 0.5$. Particles are grouped into bins by radius of width 0.4 μm, recalling that $\delta_a = 0.1$ μm. Labels on lines indicate bin size in μm. Markers represent the bulk scalar dispersion of the suspensions, C. Lower C_j indicates particles have migrated closer to the channel mid-plane.

propagation from the sheared region must cause the smaller particles to rebound towards the channel mid-plane with a greater velocity. Consequently, as the plug grows, it is the smaller particles which will be continually forced ahead of the larger particles and into the plug.

Although not explicitly shown here, these phenomena occur for all PSDs at $\bar{\phi} \geq 0.4$. An additional observation in figure 19 is that, as $\bar{\phi}$ increases, bulk migration becomes independent of the particle distribution (i.e. the same C is attained). Here, a pressure gradient of $G = 16\,\text{MPa}\,\text{m}^{-1}$ is applied to $\bar{\phi} = 0.55$, resulting in $Re_c \approx 13$. Also plotted in figure 20 is the increase in bulk effective shear viscosity, $\bar{\eta}_s$, with $\bar{\phi}$. Comparison is made with the theoretical correlation of Krieger & Dougherty (1959), $\eta_s/\eta_f = (1 - \phi/\phi_{rcp})^{-2.5\phi_{rcp}}$, where ϕ_{rcp} is obtained using (2.13). This general approach of substituting an expression for the maximum packing fraction into an existing viscosity correlation has been highly successful (Pednekar *et al.* 2018) and reproduces a dependence on the PSD. The obtained $\bar{\eta}_s$ in figure 20 exhibit this same dependence, which becomes more pronounced at higher $\bar{\phi}$. Divergence of the simulation $\bar{\eta}_s$ from the correlation at $\bar{\phi} \geq 0.4$ occurs as the former is a channel-averaged quantity and decreases with the presence of a plug (where the mean shear rate is zero), while the correlation is for a locally sheared suspension.
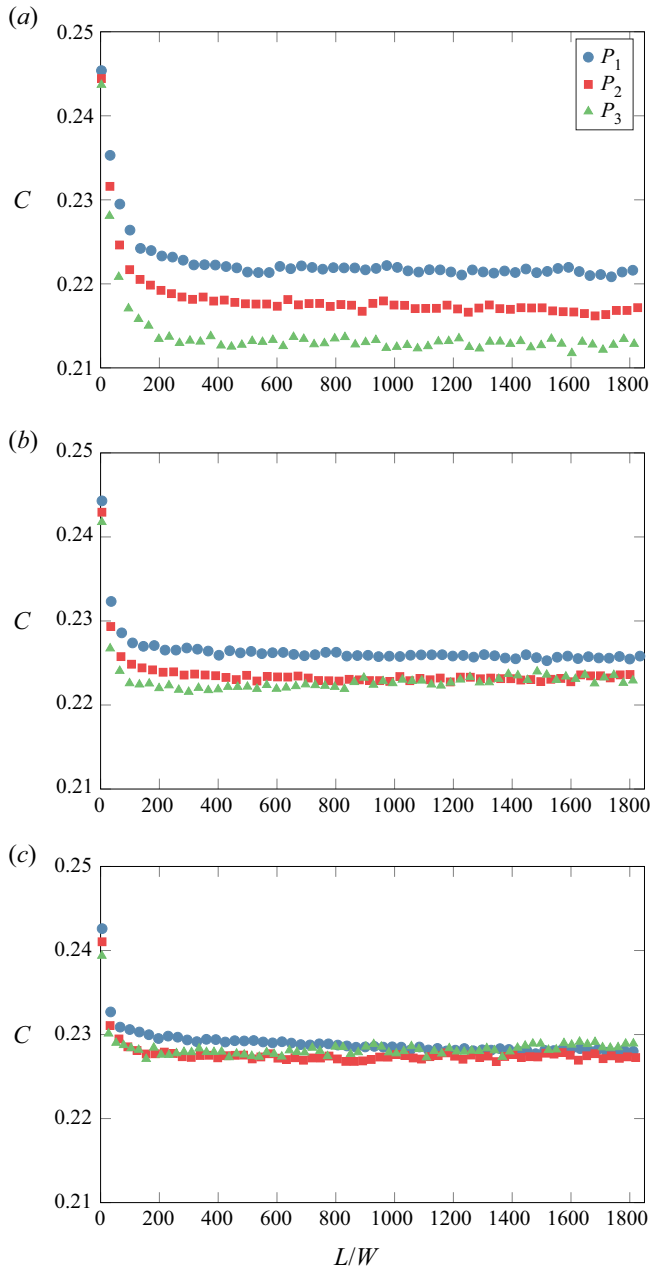
939 A30-22

Figure 19. Development of bulk migration, C, along the length of the channel, L/W, for (*a*) $\bar{\phi} = 0.4$, (*b*) $\bar{\phi} = 0.5$ and (*c*) $\bar{\phi} = 0.55$, indicating that as $\bar{\phi}$ increases, bulk migration becomes independent of the particle distribution.

3.3. *Inertia*

As outlined in § 1, suspension migration is dependent on a combination of IM and SIM, to varying degrees. Firstly, to quantify the contribution of inertia to the results in § 3.1, G is varied between values of 1, 2 and 3 MPa m^{-1} for P_2 at $\bar{\phi} = 0.3$, corresponding to $Re_c = 13$, 25 and 38. Figure 21 demonstrates an increase in bulk migration towards the channel
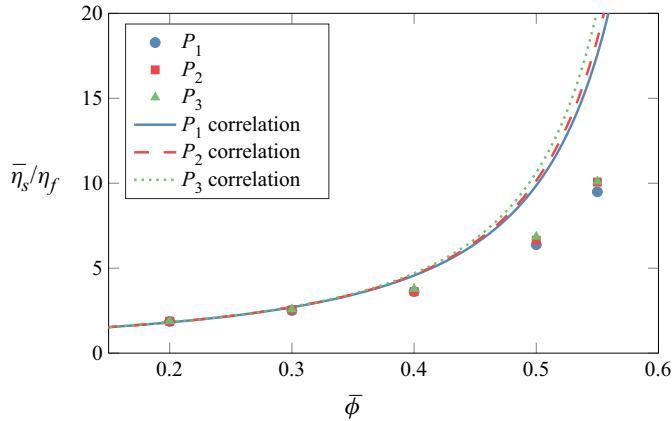
Figure 20. Increase in bulk effective shear viscosity with bulk solid volume fraction, obtained from simulations as $\bar{\eta}_s = GW^2/(12\langle u \rangle)$. Comparison with theoretical correlation of Krieger & Dougherty (1959), $\eta_s/\eta_f = (1 - \phi/\phi_{rcp})^{-2.5\phi_{rcp}}$, where ϕ_{rcp} is obtained using (2.13).
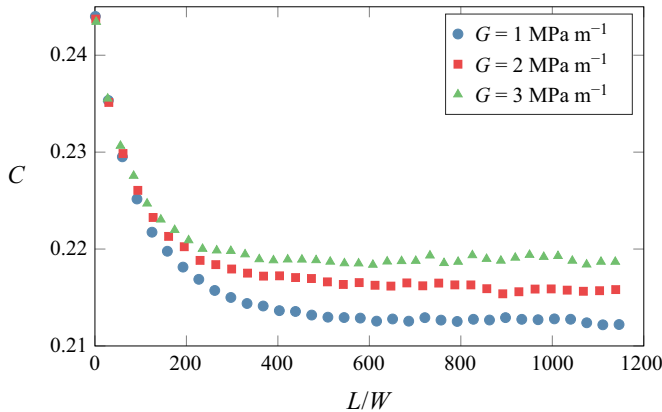

Figure 21. Development of bulk scalar dispersion function, C, along normalised channel length, L/W. Comparison of different G for P_2 at $\bar{\phi} = 0.3$, demonstrating dependence of migration on inertia at moderate $\bar{\phi}$.

walls as Re_c is increased. This is commensurate with the general effect of inertia causing particles to migrate away from the channel mid-plane. Conversely, by decreasing Re_c, IM decreases relative to SIM, causing greater bulk migration to the channel mid-plane.

Figure 22, however, shows that the largest particles attain a position closer to the channel centre as G (and hence inertia) increases, while the smallest particles migrate closer to the channel walls. This behaviour can be explained by the dependence of SIM on the particle Reynolds number, as discussed in § 1. As the particle self-diffusivity increases with Re_p (Kromkamp *et al.* 2005), it is the larger particles which will exhibit the greatest increase in SIM (and hence closest position to the mid-plane) with increasing G.

Next, to compare the effect of inertia at the higher solid volume fractions tested in § 3.2, G is varied between values of $G = 3$, 5.5, 8 and $10 \, \text{MPa m}^{-1}$ for P_2 at $\bar{\phi} = 0.5$, corresponding to $Re_c = 6$, 11, 16 and 20. Figures 23 and 24 show that the variation in bulk migration and size segregation with inertia is minimal. This is commensurate with the fact that dependence of self-diffusivity on Re_p disappears with higher $\bar{\phi}$, and also suggests that SIM is generally dominating IM due to the high particle concentration.
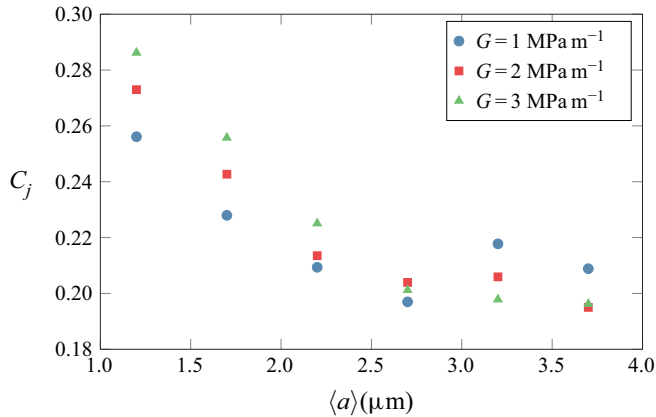
939 A30-24

Figure 22. Scalar dispersion function by particle size species, C_j. Comparison of different G at $\bar{\phi} = 0.3$ for P_2, measured at $L/W \approx 1200$. Particles are grouped into bins by particle radius of width $0.4\,\mu\text{m}$, recalling that $\delta_a = 0.1\,\mu\text{m}$, and are plotted at their median value, $\langle a \rangle$. Lower C_j indicates particles have migrated closer to the channel mid-plane.
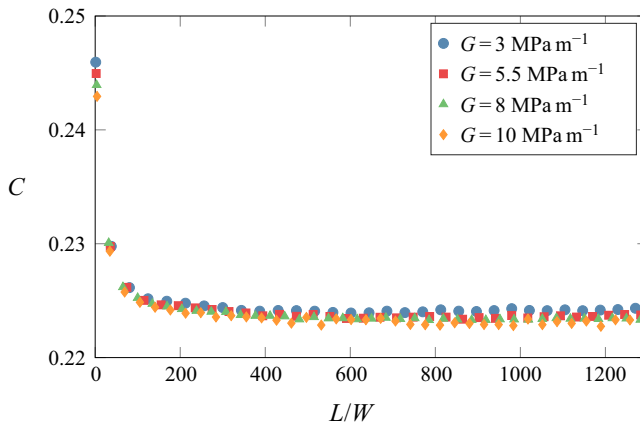

Figure 23. Development of bulk scalar dispersion function, C, along normalised channel length, L/W. Comparison of different G for P_2 at $\bar{\phi} = 0.5$, demonstrating independence of migration on inertia at high $\bar{\phi}$.

3.4. *Equivalence of bidisperse suspensions*

Here, a quantitative comparison is made between the bulk migration and size segregation of bidisperse and polydisperse suspensions, motivated by the recent finding that bidisperse and polydisperse suspensions with matching first three statistical moments (mean, variance, skewness – M_1, M_2, M_3) exhibit matching viscosity (Pednekar *et al.* 2018). To assess whether this equivalence translates to SIM in channel flows, the first three statistical moments are also used here as a measure of equivalence. Table 2 defines the five bidisperse PSDs (B_1, B_2, B_3, $B_{2,1}$, $B_{2,2}$) which are statistically equivalent to their respective polydisperse PSDs defined in § 2.3 (P_1, P_2, P_3, $P_{2,1}$, $P_{2,2}$). Therefore, M_1, M_2 and M_3 exactly match those in table 1. These moments are then defined for
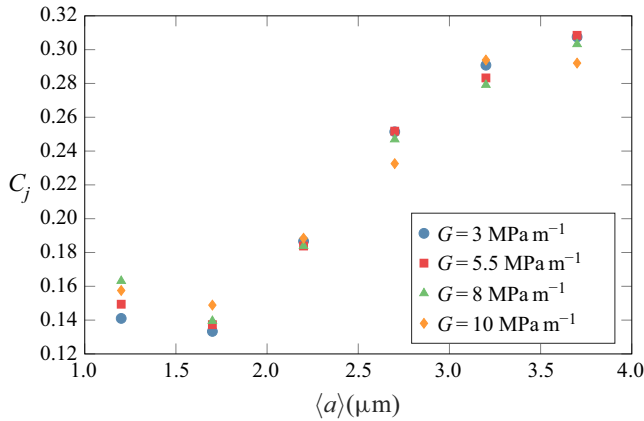
Figure 24. Scalar dispersion function by particle size species, C_j. Comparison of different G at $\bar{\phi} = 0.5$ for P_2, measured at $L/W \approx 1200$. Particles are grouped into bins by particle radius of width 0.4 μm, recalling that $\delta_a = 0.1$ μm, and are plotted at their median value, $\langle a \rangle$. Lower C_j indicates particles have migrated closer to the channel mid-plane.

	a_S	a_L	N_S	M_1	M_2	M_3	ϕ_{rcp}
B_1	1.31	2.68	0.80	1.58	0.30	1.50	0.672
B_2	1.47	2.88	0.71	1.88	0.41	0.92	0.666
B_3	1.83	3.22	0.54	2.47	0.48	0.17	0.654
$B_{2,1}$	1.40	3.07	0.71	1.89	0.58	0.9	0.673
$B_{2,2}$	1.53	2.66	0.68	1.89	0.28	0.78	0.658

Table 2. The five bidisperse PSDs used in this work, with first three statistical moments, M_1, M_2 and M_3, taken to match their respective polydisperse distributions in table 2. Equations (3.5) are then solved simultaneously to obtain the radii of small and large particles, a_S and a_L, and the number fraction of small particles, N_S. Here, ϕ_{rcp} is obtained from (2.13).

bidisperse PSDs,

$$\left. \begin{aligned} M_1 &= a_S N_S + a_L(1 - N_S), \\ M_2 &= N_S (a_S - M_1)^2 + (1 - N_S)(a_L - M_1)^2, \\ M_3 &= \left[N_S (a_S - M_1)^3 + (1 - N_S)(a_L - M_1)^3 \right] / M_2^{3/2}, \end{aligned} \right\} \tag{3.5}$$

where a_S and a_L are the radii of small and large particles, respectively, and N_S is the number fraction of small particles. To obtain a_S, a_L and N_S the system of (3.5) are simultaneously solved for each PSD by substituting the respective values of M_1, M_2 and M_3 from table 2. With matching moments ϕ_{rcp} must also be equal according to (2.13).

Firstly, the five bidisperse suspensions are simulated at constant parameters of $\bar{\phi} = 0.3$ and $G = 2\,\mathrm{MPa\,m^{-1}}$ to facilitate comparison with their equivalent polydisperse suspensions. Figure 25 shows that the bulk migration of the bidisperse suspensions matches that of the polydisperse suspensions (figure 8) remarkably closely. Consequently, it may confidently be concluded that the rheological equivalence of bidisperse and polydisperse suspensions extends to SIM in channel flows. In this way, the first three
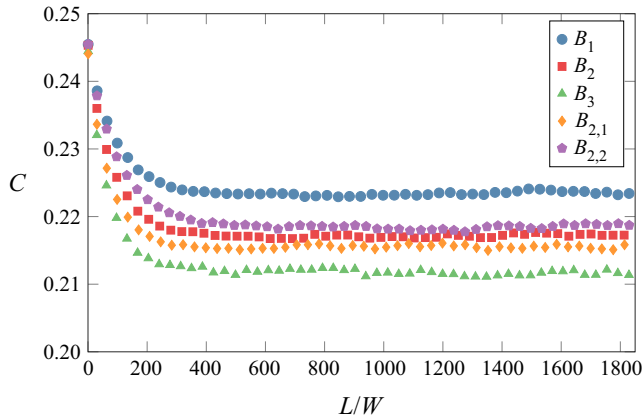
939 A30-26

Figure 25. Development of bulk scalar dispersion function, C, along normalised channel length, L/W. Comparison of each bidisperse PSD at $\bar{\phi} = 0.3$, $G = 2\,\mathrm{MPa\,m^{-1}}$, demonstrating close agreement to the bulk migration of their respective polydisperse suspensions in figure 8.

statistical moments must also completely describe the shear-induced diffusivity of a suspension. By extension, this supports the theory that a classical homogeneous rheology description of SIM, such as the effective temperature SBM approach for bidisperse suspensions (van der Sman & Vollebregt 2012), can be extended to polydisperse suspensions, with the only requirement being adequate closure relations. It is acknowledged, however, that this result is obtained empirically, for a relatively narrow set of distributions. Consequently, generalisation remains to be shown.

Notwithstanding these similarities, two primary differences between figures 25 and 8 are evident: firstly, C is slightly higher for the bidisperse results compared with the polydisperse, meaning slightly less bulk migration to the channel mid-plane; and secondly, the bidisperse PSDs with matching mean (B_2, $B_{2,1}$, $B_{2,2}$) are all slightly closer compared with their equivalent polydisperse PSDs (P_2, $P_{2,1}$, $P_{2,2}$). This suggests that there exists some minor dependence on polydispersity which is not recovered in a bidisperse approximation. One likely cause of this is that the size ratio of smallest-to-largest particles in the polydisperse suspensions is larger than in the bidisperse suspensions, which is an inherent requirement of statistical equivalence.

Finally, the effect of bulk solid volume fraction on bidisperse SIM is investigated by simulating bulk concentrations of $\bar{\phi} = 0.2$, 0.3, 0.4 and 0.5 for B_2 only. As with the polydisperse suspensions, the pressure gradient is increased with $\bar{\phi}$ as $G = 1.1$, 2, 4.25 and $10\,\mathrm{MPa\,m^{-1}}$ to obtain a similar Re_c for all $\bar{\phi}$ ($Re_c = 25$, 25, 25 and 20). Development of the bulk migration and segregation of individual size species are shown in figure 26. As for the dependence on PSD shown above, the bidisperse dependence on concentration agrees nearly exactly with the polydisperse dependence on concentration (figure 14). The velocity profiles in figure 27 also demonstrate the formation of a plugged region at $\bar{\phi} = 0.5$, which is slightly smaller compared with that of the polydisperse suspension, while it appears that no plug exists at $\bar{\phi} = 0.4$. Analogous to the polydisperse suspensions, however, the small particles primarily form the plug at $\bar{\phi} = 0.5$ and migrate closest to the channel centre, even in this case where only two particle size species are present. This is reflected in figure 26, where the C_j of the smallest and largest particles cross over at $L/W \approx 400$, as well as in the rendering of figure 28.
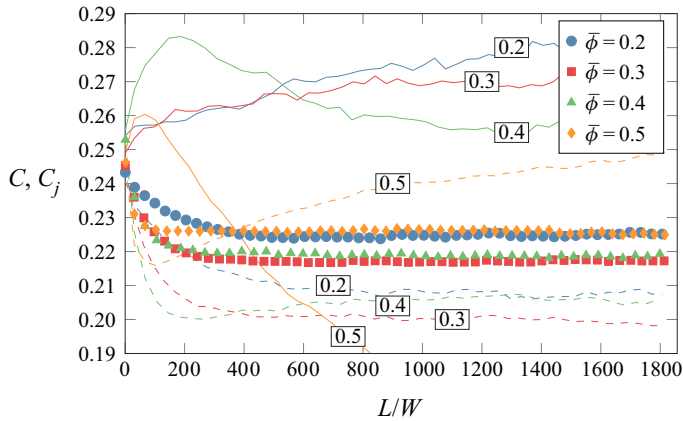
Figure 26. Development of bulk scalar dispersion function, C, along normalised channel length, L/W. Comparison of different $\bar{\phi}$ for B_2, demonstrating close agreement with the dependence of bulk migration on $\bar{\phi}$ for P_2 (figure 14). Solid lines represent C_j of small particles and dashed lines represent C_j of large particles. Lines are labelled by their $\bar{\phi}$ for further clarity. Crossing over of C_j for $\bar{\phi}$ indicates small particles have migrated closer to the channel mid-plane on average compared with large particles.
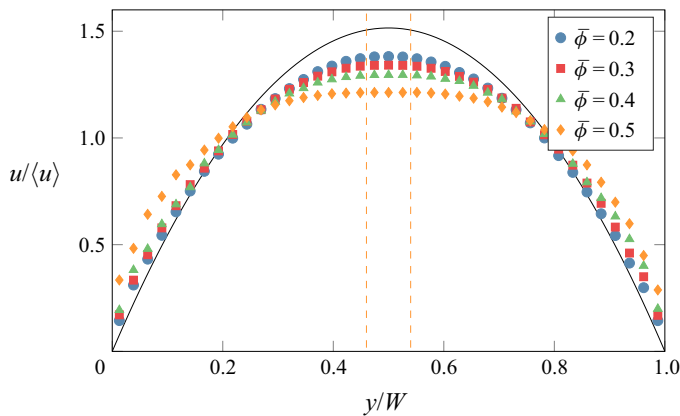

Figure 27. Comparison of velocity profiles for increasing $\bar{\phi}$ for B_2, measured at $L/W \approx 1800$. Vertical dashed lines indicate the plugged region for $\bar{\phi} = 0.5$.
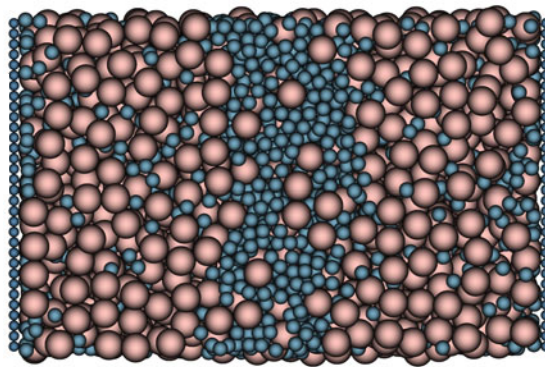

Figure 28. Graphical representation of $\bar{\phi} = 0.5$ for B_2, captured at $L/W \approx 1800$, illustrating closer migration to the channel mid-plane of small particles compared with large particles.

939 A30-28

4. Conclusions

The present work examines the bulk migration and size segregation behaviour of continuously distributed (polydisperse), dense particle suspensions in pressure-driven, planar channel flows. General dependence of bulk migration and size segregation on the distributions is shown, which is described by a dual dependence on the particle self-diffusivity and viscous suspension reordering; the largest particles will preferentially migrate to the channel mid-plane due to quadratic scaling of the self-diffusivity with particle size, which is in turn constrained by the local rheology imposed by the particle pressure gradient. For $\bar{\phi} = 0.3$ reordering occurs on a length scale of 1.3–3 times longer than the initial shear-induced diffusion. Based on the recent finding that suspension rheology can be characterised by the first three statistical moments of a particle size distribution, the suspensions here are characterised in the same manner. By demonstrating close agreement between the bulk migration of equivalent bidisperse and polydisperse suspensions, it is confirmed that the statistical moments completely characterise a suspension's migration, and by extension its shear-induced diffusivity.

At bulk suspension concentrations of $\bar{\phi} > 0.3$, the formation of a plugged region at the channel centre occurs on the same length scale as suspension bulk migration, and determines the size of the sheared (outer) regions of the channel. The smallest particles of the suspension preferentially form the plugs, causing the largest particles to migrate into the sheared regions at the channel walls. As $\bar{\phi}$ increases and the plug size increases, more small particles are required to compose the plug, meaning that more large particles will segregate closer to the channel walls. This behaviour has not been observed in the literature hitherto, and also occurs in bidisperse suspensions where only two particle sizes are present. It is theorised that small particles preferentially form the plugs due to their higher shear-rate fluctuations, which completely dominate particle motion near the plug where the mean shear rate vanishes.

Finally, the competing migration towards and away from the channel mid-plane due to shear-induced migration and inertia, respectively, cause a greater bulk migration to the walls as inertia is increased. Dependence of the particle self-diffusivity on the particle Reynolds number, however, results in increased mid-plane migration for the largest particles as inertia increases. These dependencies on inertia disappear as the bulk solid volume fraction increases and shear-induced migration dominates. Similarly, dependence on the PSD disappears as the bulk solid volume fraction increases.

Declaration of interests. The authors report no conflict of interest.

Author ORCIDs.

- Nathan J. Di Vaira https://orcid.org/0000-0002-1302-4859;
- Łukasz Łaniewski-Wołłk https://orcid.org/0000-0002-3026-5881;
- Raymond L. Johnson Jr. https://orcid.org/0000-0002-0659-3770;
- Saiied M. Aminossadati https://orcid.org/0000-0001-8385-3444;
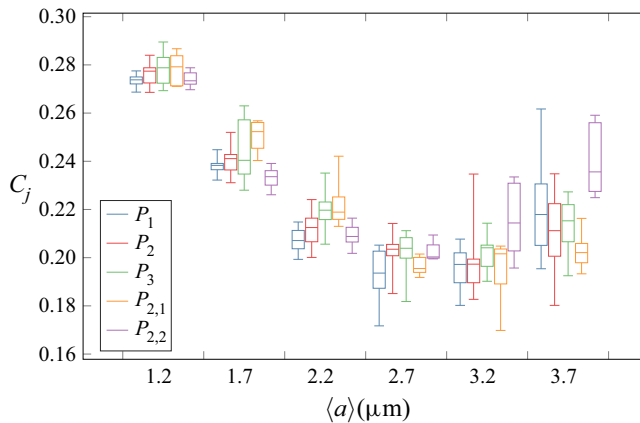- Christopher R. Leonardi https://orcid.org/0000-0001-8596-9125.

Figure 29. Reproduction of figure 11 showing statistic quartiles of C_j for each PSD in each particle size bin. Each PSD is simulated ten times with randomised particle injection seeding.

Appendix

As described in § 2.3 SIM is stochastic in nature, which manifests in variation of the bulk migration and size segregation between simulations with identical parameters but randomised particle injection seeding. Figure 29 exemplifies this for the case of C_j of each PSD, showing the statistic quartiles. These data were originally presented in figure 11, showing only the median C_j for each point. In this case, ten different simulations with randomised particle injection seeding are utilised for each PSD.

REFERENCES

ABBAS, M., MAGAUD, P., GAO, Y. & GEOFFROY, S. 2014 Migration of finite sized particles in a laminar square channel flow from low to high Reynolds numbers. *Phys. Fluids* **26** (12), 123301.

BURNS, S.J., PIIROINEN, P.T. & HANLEY, K.J. 2019 Critical time step for DEM simulations of dynamic systems using a Hertzian contact model. *Intl J. Numer. Meth. Engng* **119** (5), 432–451.

CHANG, C. & POWELL, R.L. 1994 The rheology of bimodal hard-sphere dispersions. *Phys. Fluids* **6** (5), 1628–1636.

CHUN, B., KWON, I., JUNG, H.W. & HYUN, J.C. 2017 Lattice Boltzmann simulation of shear-induced particle migration in plane Couette–Poiseuille flow: local ordering of suspension. *Phys. Fluids* **29** (12), 121605.

CHUN, B., PARK, J.S., JUNG, H.W. & WON, Y. 2019 Shear-induced particle migration and segregation in non-Brownian bidisperse suspensions under planar Poiseuille flow. *J. Rheol.* **63** (3), 437–453.

CHUN, J., OH, T., LUNA, M. & SCHWEIGER, M. 2011 Effect of particle size distribution on slurry rheology: nuclear waste simulant slurries. *Colloids Surf.* A **384** (1), 304–310.

COOK, B., NOBLE, D. & WILLIAMS, J. 2004 A direct simulation method for particle-fluid systems. *Engng Comput.* **21**, 151–168.

CUNDALL, P.A. & STRACK, O.D.L. 1979 A discrete numerical model for granular assemblies. *Géotechnique* **29** (1), 47–65.

DESMOND, K.W. & WEEKS, E.R. 2014 Influence of particle size distribution on random close packing of spheres. *Phys. Rev.* E **90**, 022204.

VAN DINTHER, A.M.C., SCHROËN, C.G.P.H., IMHOF, A., VOLLEBREGT, H.M. & BOOM, R.M. 2013 Flow-induced particle migration in microchannels for improved microfiltration processes. *Microfluid Nanofluidics* **15** (4), 451–165.

FAXEN, H. 1923 Die bewegung einer starren kugel längs der achse eines mit zäher flussigkeit gefülten rohres. PhD thesis, Uppsala University.

GILLISSEN, J.J.J. & NESS, C. 2020 Modeling the microstructure and stress in dense suspensions under inhomogeneous flow. *Phys. Rev. Lett.* **125**, 184503.

Gu, Y., Ozel, A. & Sundaresan, S. 2016 Rheology of granular materials with size distributions across dense-flow regimes. *Powder Technol.* **295**, 322–329.

Guazzelli, É. & Pouliquen, O. 2018 Rheology of dense granular suspensions. *J. Fluid Mech.* **852**, P1.

Han, K., Feng, Y.T. & Owen, D.R.J. 2007 Coupled lattice Boltzmann and discrete element modelling of fluid–particle interaction problems. *Comput. Struct.* **85** (11), 1080–1088. fourth MIT Conference on Computational Fluid and Solid Mechanics.

Henriquez Rivera, R.G., Zhang, X. & Graham, M.D. 2016 Mechanistic theory of margination and flow-induced segregation in confined multicomponent suspensions: simple shear and poiseuille flows. *Phys. Rev. Fluids* **1**, 060501.

Holdych, D.J., Noble, D.R., Georgiadis, J.G. & Buckius, R.O. 2004 Truncation error analysis of lattice Boltzmann methods. *J. Comput. Phys.* **193** (2), 595–619.

Jenkins, J.T. & McTigue, D.F. 1990 Transport processes in concentrated suspensions: the role of particle fluctuations. In *Two Phase Flows and Waves* (ed. D.D. Joseph & D.G. Schaeffer), pp. 70–79. Springer.

Kazerooni, H.T., Fornari, W., Hussong, J. & Brandt, L. 2017 Inertial migration in dilute and semidilute suspensions of rigid particles in laminar square duct flow. *Phys. Rev. Fluids* **2**, 084301.

Kloss, C., Goniva, C., Hager, A., Amberger, S. & Pirker, S. 2012 Models, algorithms and validation for opensource DEM and CFD-DEM. *Prog. Comput. Fluid Dyn.* **12** (2/3), 140–152.

Krieger, I.M. & Dougherty, T.J. 1959 A mechanism for non-newtonian flow in suspensions of rigid spheres. *Trans. Soc. Rheol.* **3** (1), 137–152.

Kromkamp, J., van den Ende, D.T.M., Kandhai, D., van der Sman, R.G.M. & Boom, R.M. 2005 Shear-induced self-diffusion and microstructure in non-Brownian suspensions at non-zero Reynolds numbers. *J. Fluid Mech.* **529**, 253–278.

Kromkamp, J., van den Ende, D., Kandhai, D., van der Sman, R. & Boom, R. 2006 Lattice Boltzmann simulation of 2D and 3D non-Brownian suspensions in Couette flow. *Chem. Engng Sci.* **61** (2), 858–873.

Kromkamp, J., van Domselaar, M., Schroën, K., van der Sman, R. & Boom, R. 2002 Shear-induced diffusion model for microfiltration of polydisperse suspensions. *Desalination* **146** (1), 63–68.

Kruger, T., Kusumaatmaja, H., Kuzmin, A., Shardt, O., Silva, G. & Viggen, E.M. 2017 *The Lattice Boltzmann Method – Principles and Practice*. Springer International Publishing.

Łaniewski-Wołłk, Ł. 2017 Topology optimization and optimal control using adjoint lattice Boltzmann method. Doctor of philosophy, Warsaw University of Technology.

Łaniewski-Wołłk, Ł. & Leonardi, C. 2020 Towards a stochastic model of the permeability of rough fractures. In *Proceedings of the 22nd Australasian Fluid Mechanics Conference AFMC2020* (ed. H. Chanson & R. Brown). The University of Queensland.

Łaniewski-Wołłk, Ł. & Rokicki, J. 2016 Adjoint lattice Boltzmann for topology optimization on multi-GPU architecture. *Comput. Maths Applics.* **71** (3), 833–848.

Lecampion, B. & Garagash, D.I. 2014 Confined flow of suspensions modelled by a frictional rheology. *J. Fluid Mech.* **759**, 197–235.

Leighton, D. & Acrivos, A. 1987 The shear-induced migration of particles in concentrated suspensions. *J. Fluid Mech.* **181**, 415–439.

Luckham, P.F. & Ukeje, M.A. 1999 Effect of particle size distribution on the rheology of dispersed systems. *J. Colloid Interface Sci.* **220** (2), 347–356.

Lyon, M.K. & Leal, L.G. 1998a An experimental study of the motion of concentrated suspensions in two-dimensional channel flow. Part 1. Monodisperse systems. *J. Fluid Mech.* **363**, 25–56.

Lyon, M.K. & Leal, L.G. 1998b An experimental study of the motion of concentrated suspensions in two-dimensional channel flow. Part 2. Bidisperse systems. *J. Fluid Mech.* **363**, 57–77.

Matas, J., Morris, J.F. & Guazzelli, É. 2004 Inertial migration of rigid spherical particles in Poiseuille flow. *J. Fluid Mech.* **515**, 171–195.

McCullough, J.W.S., Leonardi, C.R., Jones, B.D., Aminossadati, S.M. & Williams, J.R. 2016 Lattice Boltzmann methods for the simulation of heat transfer in particle suspensions. *Intl J. Heat Fluid Flow* **62**, 150–165.

Medina, R., Detwiler, R.L., Prioul, R., Xu, W. & Elkhoury, J.E. 2018 Effect of flow geometry on the evolution of concentrated suspensions flowing through a fracture. *Intl J. Multiphase Flow* **108**, 80–92.

Miller, R.M. & Morris, J.F. 2006 Normal stress-driven migration and axial development in pressure-driven flow of concentrated suspensions. *J. Non-Newtonian Fluid Mech.* **135** (2), 149–165.

Müller, K., Fedosov, D.A. & Gompper, G. 2016 Understanding particle margination in blood flow – a step toward optimized drug delivery systems. *Med. Engng Phys.* **38** (1), 2–10.

MORRIS, J.F. & BOULAY, F. 1999 Curvilinear flows of noncolloidal suspensions: the role of normal stresses. *J. Rheol.* **43** (5), 1213–1237.

MORRIS, J.F. & BRADY, J.F. 1998 Pressure-driven flow of a suspension: buoyancy effects. *Intl J. Multiphase Flow* **24** (1), 105–130.

NOBLE, D.R. & TORCZYNSKI, J.R. 1998 A lattice-Boltzmann method for partially saturated computational cells. *Intl J. Mod. Phys.* C **09** (08), 1189–1201.

NOTT, P.R. & BRADY, J.F. 1994 Pressure-driven flow of suspensions: simulation and theory. *J. Fluid Mech.* **275**, 157–199.

OH, S., SONG, Y., GARAGASH, D.I., LECAMPION, B. & DESROCHES, J. 2015 Pressure-driven suspension flow near jamming. *Phys. Rev. Lett.* **114**, 088301.

OWEN, D.R.J., LEONARDI, C.R. & FENG, Y.T. 2011 An efficient framework for fluid–structure interaction using the lattice Boltzmann method and immersed moving boundaries. *Intl J. Numer. Meth. Engng* **87** (1–5), 66–95.

PÄHTZ, T., DURÁN, O., DE KLERK, D.N., GOVENDER, I. & TRULSSON, M. 2019 Local rheology relation with variable yield stress ratio across dry, wet, dense, and dilute granular flows. *Phys. Rev. Lett.* **123**, 048001.

PEDNEKAR, S., CHUN, J. & MORRIS, J.F. 2018 Bidisperse and polydisperse suspension rheology at large solid fraction. *J. Rheol.* **62** (2), 513–526.

PHILLIPS, R.J., ARMSTRONG, R., BROWN, R., GRAHAM, A. & ABBOTT, J.R. 1992 A constitutive equation for concentrated suspensions that accounts for shear-induced particle migration. *Phys. Fluids* **4**, 30–40.

POCOCK, G., RICHARDS, C.D., RICHARDS, D. & RICHARDS, D.A. 2013 *Human Physiology*. Oxford University Press.

RASTOGI, S.R., WAGNER, N.J. & LUSTIG, S.R. 1996 Microstructure and rheology of polydisperse, charged suspensions. *J. Chem. Phys.* **104** (22), 9249–9258.

REDDY, M.M. & SINGH, A. 2019 Shear-induced particle migration and size segregation in bidisperse suspension flowing through symmetric t-shaped channel. *Phys. Fluids* **31** (5), 053305.

RETTINGER, C. & RÜDE, U. 2018 A coupled lattice Boltzmann method and discrete element method for discrete particle simulations of particulate flows. *Comput. Fluids* **172**, 706–719.

SEMWOGERERE, D. & WEEKS, E.R. 2008 Shear-induced particle migration in binary colloidal suspensions. *Phys. Fluids* **20** (4), 043306.

SHAULY, A., WACHS, A. & NIR, A. 1998 Shear-induced particle migration in a polydisperse concentrated suspension. *J. Rheol.* **42** (6), 1329–1348.

VAN DER SMAN, R.G.M. & VOLLEBREGT, H.M. 2012 Effective temperature for sheared suspensions: a route towards closures for migration in bidisperse suspension. *Adv. Colloid Interface Sci.* **185–186**, 1–13.

STRACK, O.E. & COOK, B. 2007 Three-dimensional immersed boundary conditions for moving solids in the lattice Boltzmann method. *Intl J. Numer. Meth. Fluids* **55**, 103–125.

VOLLEBREGT, H.M., VAN DER SMAN, R.G.M. & BOOM, R.M. 2012 Model for particle migration in bidisperse suspensions by use of effective temperature. *Faraday Discuss.* **158**, 89–103.

VOLLEBREGT, H.M., VAN DER SMAN, R.G.M. & BOOM, R.M. 2010 Suspension flow modelling in particle migration and microfiltration. *Soft Matt.* **6**, 6052–6064.

WANG, D., LEONARDI, C.R. & AMINOSSADATI, S.M. 2018 Improved coupling of time integration and hydrodynamic interaction in particle suspensions using the lattice boltzmann and discrete element methods. *Comput. Maths Applics.* **75** (7), 2593–2606.

YANG, G.C., JING, L., KWOK, C.Y. & SOBRAL, Y.D. 2019 A comprehensive parametric study of LBM-DEM for immersed granular flows. *Comput. Geotech.* **114**, 103100.

YEO, K. & MAXEY, M.R. 2011 Numerical simulations of concentrated suspensions of monodisperse particles in a poiseuille flow. *J. Fluid Mech.* **682**, 491–518.

ZHOU, J., MUKHERJEE, P., GAO, H., LUAN, Q. & PAPAUTSKY, I. 2019 Label-free microfluidic sorting of microparticles. *APL Bioengng* **3** (4), 041504.